



**HAL**  
open science

## Durability assessment and microstructural analysis of 3D printed concrete exposed to sulfuric acid environments

Bilal Baz, Georges Aouad, Joelle Kleib, David Bulteel, Sébastien Rémond

### ► To cite this version:

Bilal Baz, Georges Aouad, Joelle Kleib, David Bulteel, Sébastien Rémond. Durability assessment and microstructural analysis of 3D printed concrete exposed to sulfuric acid environments. *Construction and Building Materials*, 2021, 290, pp.123220. 10.1016/j.conbuildmat.2021.123220 . hal-03252535

**HAL Id: hal-03252535**

**<https://hal.science/hal-03252535>**

Submitted on 24 Apr 2023

**HAL** is a multi-disciplinary open access archive for the deposit and dissemination of scientific research documents, whether they are published or not. The documents may come from teaching and research institutions in France or abroad, or from public or private research centers.

L'archive ouverte pluridisciplinaire **HAL**, est destinée au dépôt et à la diffusion de documents scientifiques de niveau recherche, publiés ou non, émanant des établissements d'enseignement et de recherche français ou étrangers, des laboratoires publics ou privés.



Distributed under a Creative Commons Attribution - NonCommercial 4.0 International License

# Durability assessment and microstructural analysis of 3D Printed concrete exposed to sulfuric acid environments

Bilal BAZ<sup>1,2</sup>, Georges AOUAD<sup>1</sup>, Joelle KLEIB<sup>2</sup>, David BULTEEL<sup>2</sup>, Sébastien REMOND<sup>3</sup>

<sup>1</sup> Faculty of Engineering, University Of Balamand, UOB, Al Koura, Lebanon

<sup>2</sup> IMT Lille Douai, LGCgE – GCE, F-59508 Douai, France

<sup>3</sup> Univ Orléans, Univ Tours, INSA CVL, LaMé, EA 7494, France

## Abstract

Additive manufacturing techniques are being more adopted in the construction field, and they are rapidly developing. However, it is expected that layers superposition imposes several limitations on the performance of 3D printed structures. In this regard, an efficient concrete structure should not only present reliable mechanical performances, but also appropriate durability performance against weathering. This paper presents an experimental study aiming to compare 3D printed elements to casted ones on a macro and micro scale, as well as their resistance against sulfuric acid attacks. Herein, three different mortar mixes having different thixotropic properties were used, and two solution concentrations were employed, one containing 1% sulfuric acid and the other containing 3%. At first, a visual observation of the degraded samples and their mass loss were held. Then, a microstructural characterization was performed through mercury intrusion porosimetry (MIP) and scanning electron microscopy (SEM) analyses. Still, not any printed element has cracked at the inter-layer level. Moreover, on a microscopic level, the MIP results showed that all samples of different compositions have an equal total porosity. However, the pore size distribution and their morphology largely differs between printed and non-printed specimens. The pore sizes are more spread in printed specimens. As for the SEM results, it can be clearly seen that no interface have revealed the formation of a weak plane that might even threaten the durability of the printed elements. Yet, a strong link between superposed layers has been developed, even when using materials having different rheological properties; and the overall specimen acted as a monolithic body without showing any signs of discontinuity or superposition effects.

**Keywords:** 3D printing – Durability – Mortar – Rheology – Thixotropy – Microstructural analysis – Porosity – Sulfuric acid.

## 1- Introduction

Nowadays, 3D printing is experiencing an exponential increase in terms of research and application activities, and it is continuously advancing [1]–[7]. Above all, 3D printing has been widely developed in the construction field [8], where it presented significant benefits in terms of higher geometrical freedom of concrete products, as well as faster production and lower cost [9]–[13].

40 Additive manufacturing has a remarkable impact on concrete manufacturing. Its application has  
41 evolved from printing prototypes and laboratory scale objects to the manufacturing of fully  
42 functional concrete elements [14], [15]. Recently, 3D printing of concrete elements has been  
43 applied in the infrastructure construction industry, which could bring in significant  
44 improvements to the field [16], [17]. Over and above, 3D printing was introduced to a more  
45 critical field of applications, where printed structures are continuously exposed to aggressive  
46 environments. For example, Winsun released the very first 3D printed river revetment wall, over  
47 500 meters long [18]. Similarly, XtreeE has used 3D printing technology to reproduce natural  
48 coral reefs, using normal concrete material, as well as water collectors for drainage systems [19].

49 Despite that, daily applications still seem far away because of the conservative practices in this  
50 field [3]. They are persisting challenges in penetrating the market due to the lack of compliance  
51 with building codes [20]. In addition, some technical challenges need to be overcome to trigger  
52 all the opportunities offered by 3D printing techniques in the building sector, such as  
53 reinforcement incorporation to provide sufficient tensile capacity and ductility for the intended  
54 applications [21]–[25]. Though, in order to consider 3D printing as a successful construction  
55 practice, high quality properties of the final product have to be targeted. In other words, the  
56 design of concrete elements should be based on different requirements [26], mainly specified by  
57 the structural stability and ability to bear and transfer loads [27], the durability against  
58 environmental effects [28], [29], and the aesthetic needs [30]. Indeed, for a broader field of  
59 applications, not just the physical and mechanical properties of printable materials need to be  
60 assessed, but the durability needs to be addressed as well. This is said because the life cycle  
61 assessment of constructions is majorly affected by the materials production [31], enabling them  
62 to reach a reasonable service life in natural or industrial exposure conditions [3].

63 The lack of performance testing protocols of 3D printed elements makes the analogy between  
64 printed and casted concrete elements obscure. All structural and durability design standards  
65 consider concrete as a homogeneous material [32], which might not be always applicable for 3D  
66 printed elements. In fact, these elements have anisotropic behavior due their particular  
67 production identity [33]–[35]. Thus, the current standards need to be revised and adapted for  
68 structures having anisotropic properties.

69 The properties of hardened cement paste are majorly influenced by its microstructure, and the  
70 way in which the material is casted [36]. The induced heterogeneities and interfaces caused by  
71 the process represent a major challenge [37]. The effect of weak interfaces between successive  
72 layers on the mechanical properties of 3D printed elements has been widely reported in the  
73 literature [38]–[42]. This weakness is due to the layered concept creating extra voids between  
74 successive layers, with more porous properties of the layers themselves, in addition to the  
75 anisotropic characteristics [3]. Having said that, the quality of the bond generated between  
76 superposed layers is mostly influenced by the rheological and thixotropic properties of the  
77 material used [7], [43], [44]. Alongside, the same printing parameters affecting the mechanical  
78 and rheological properties of concrete in its fresh and hardened states, affect the durability  
79 properties. These parameters are mainly the printing speed and pumping pressure [39]. For  
80 example, a higher print-time interval decrease the adhesion between successive layers due to the

81 water evaporation causing a lower surface moisture content and possibly a weaker bond between  
82 layers [44]. In addition, an increase in the printing speed introduces bigger pores [45]. Alongside,  
83 a lower printing pressure induces a higher surface roughness due to the kinetic energy of the sand  
84 particles causing more voids formation [46]. In some cases, air bubbles present inside the layer  
85 itself might escape due to the pressure exerted by subsequent layers and stay entrapped at the  
86 interface level. Therefore, a weak link between successive layers would threaten the durability of  
87 printed elements, due to the creation of another preferential ingress path for aggressive  
88 substances from the surrounding environment. Alternatively stated, the chemical diffusion  
89 through interfaces can be faster than that in bulk concrete, which may jeopardize the durability of  
90 the structure. In addition, this matter would increase the corrosion rate of the reinforcing steel  
91 bars placed between layers. However, the current focus on the material properties concerning the  
92 durability aspect is still limited [32].

93 Durability characteristics correspond to the ability of the material to resist different  
94 environmental exposures for a long period of time, without significant deterioration [47].  
95 Concerning the durability of concrete material, it depends on many factors, mainly cement type  
96 and content, water to cement (W/C) ratio [7], [48], curing conditions and compaction [49].  
97 Indeed, some of these aspects are not relevant for 3D printed elements, especially those related to  
98 compaction, which is not applicable in the field of additive manufacturing.

99 Typically, it is known that ordinary Portland cement has little resistance to acid attacks, because  
100 of its high alkalinity [50], [51]. Therefore, acids can easily deteriorate concrete in various ways.  
101 Notably, sulfuric acid ( $H_2SO_4$ ) is one of the most harmful acids to act on concrete materials due  
102 to its combined effect of acid and sulphate attack [52]. It reacts with the calcium hydroxide (CH)  
103 of the hydrated cement paste, and produces gypsum. Yet, the decomposition of concrete under  
104 acid attack depends mainly on concrete porosity and acid concentration [53].

105 This study is based on an experimental analysis of concrete samples exposed to sulfuric acid  
106 environments. Though, it is less common for a 3D printed structure to be subjected to high  
107 concentrations of acid attacks; however, the reason behind using it is because of being very  
108 corrosive, and thus, it would considerably accelerate the corrosion rate of concrete samples.  
109 However, the objective of this research is to investigate the microstructural properties of 3D  
110 printed concrete elements and their resistance against sulfuric acid attacks, in comparison to non-  
111 printed samples. In particular, it aims to qualify the interfaces and bonding efficiency between  
112 successive layers. Hence, it aims to draw a better perception regarding whether a printed element  
113 acts homogeneously as a casted object, or as a stack of concrete layers. Herein, three mixes  
114 compositions having different thixotropic properties were used, and all specimens whether  
115 printed or not, were studied on a macroscopic and microscopic scale.

## 116 2- Materials and Methods

117 The experimental program presented in this research covers two phases. The first phase  
118 corresponds to the materials development and rheological characterizations, whereas the second  
119 one describes the production and preparation of the specimens used for the durability assessment.

120 **2.1- Mix design and material characterization**

121 **2.1.1- Raw Materials**

122 All developed mixes consisted of an Ordinary Portland Cement (CEM I 52.5 N), having a  
123 density of 3.1g/cm<sup>3</sup> and 8.2 μm median particle diameter “D<sub>50</sub>”. The sand used was made of  
124 crushed limestone having a particle size distribution of 0 to 2 mm including 19% smaller than 63  
125 μm and a density of 2.7 g/cm<sup>3</sup>. These mixes contained as well CBCALC 80 μm limestone filler  
126 with a density of 2.7g/cm<sup>3</sup> and 5.7 μm D<sub>50</sub>. As for the admixtures used, all mixes contained  
127 CHRYSO®Fluid Optima 100 high range water reducer (HRWR) having a phosphonate base  
128 with 31% ± 1.5% dry content, and a commercially used BELITEX® ADDICHAP viscosity  
129 modifying agent (VMA) powder.

130 The chemical composition of the cement are shown in table 1.

131 *Table 1: Chemical composition of cement*

<b>Compounds</b>	<b>Concentration (%)</b>
CaO	63.8
SiO <sub>2</sub>	20.0
Al <sub>2</sub> O <sub>3</sub>	5.3
Fe <sub>2</sub> O <sub>3</sub>	3.0
SO <sub>3</sub>	3.0
MgO	0.9
K <sub>2</sub> O	0.9
Na <sub>2</sub> O	0.5
P <sub>2</sub> O <sub>5</sub>	0.3
TiO <sub>2</sub>	0.3
MnO	< 0.1
NiO	< 0.1
CuO	< 0.1
ZnO	0.1
SrO	0.1
ZrO <sub>2</sub>	< 0.1

132

133 **2.1.2- Mortar compositions**

134 Three mixes having different thixotropic characteristics were used in this study. In particular, this  
135 was done because previous researches have confirmed that the rheological and thixotropic  
136 properties of the printable materials could affect the quality of the bond generated between  
137 superposed layers [54]–[56]. If this were to happen, weak plane could be formed creating  
138 preferential pathways for chemicals intrusion. Therefore, the aim of testing more than one  
139 composition was to exclusively investigate the overall effect of 3D printing techniques on the  
140 quality of the link between successive layers over a wider range of material’s conditions.

141 These mixes compositions are shown in table 2. Mix A is considered as reference, Mix B  
142 contains a higher amount of limestone filler, and Mix C has a lower water to cement ratio (W/C).

143 *Table 2: Relative mixes compositions*

	<b>Sand (S/C)</b>	<b>Filler (F/C)</b>	<b>Water (W/C)</b>	<b>VMA % (VMA/C)</b>	<b>HRWR % (HRWR/C)</b>
<b>Mix A</b>	1.72	0.33	0.51	0.40	0.81
<b>Mix B</b>	2.02	0.54	0.60	0.47	0.95
<b>Mix C</b>	1.72	0.33	0.41	0.40	1.52

144

### 145 2.1.3- Mixing procedure

146 For the development of the mixes, a 5 liters mixer (Hobart mixer N50CE) was used, and the mixing  
147 procedure was done at room temperature ( $\approx 22^{\circ}\text{C} \pm 2^{\circ}\text{C}$ ) to minimize the difference between batches.

148 The same mixing procedure adopted by Baz et al. [57] was followed, and it consisted first of dry mixing  
149 all solid ingredients for 120 sec at a speed of 60 RPM. Water and HRWR were added gradually  
150 afterwards, during 30 sec, while keeping on the same mixing speed. Then after, the mixing speed was  
151 increased to 124 RPM for 90 sec. Once finished, the mix is left at rest for 60 sec. At the end, the  
152 material's mixing was resumed for 120 sec at 124 RPM.

### 153 2.1.4- Printability assessment

154 The printability of the developed mixes has been systematically assessed, based on visual  
155 inspections. Initially, the printing has been done manually using a laboratory gun device  
156 equipped by a circular nozzle of a 1 cm diameter, as in El Cheikh et al. [58]. Herein, the  
157 extrudability of the mortar was evaluated based on its ability to get out of the nozzle smoothly,  
158 without any discontinuity in the layer or blockage of the nozzle. Alongside, the buildability of all  
159 mortars has been evaluated based on the ability of the printed layers to stand strong and still  
160 without showing any shape deformation after the layers superposition. Fig. 1 shows a manually  
161 printed section using Mix A presenting 15 superposed layers of 1 cm thick each, having a  
162 straight wall shape.

163 Note that, the printability of all mixes used in terms of extrudability and buildability has been  
164 further confirmed using an actual 3-axis gantry printer as it is explained later in section 2.2.2.



Figure 1: Manually printed element using Mix A for printability assessment

165

166

#### 167 2.1.5- Mechanical performance of mortars

168 The mechanical performance of the newly developed mixes was systematically evaluated by  
169 measuring the compressive strength of casted (non-printed) samples at 38 days (the age when the  
170 samples were submerged in the sulfuric acid solutions for the first time). Three trials of each mix  
171 were tested at a load rate of 144 KN/min using an Instron UTM machine as per the European  
172 standard testing method NF EN 196 [59].

#### 173 2.1.6- Rheological characterization using the fall-cone test

174 The fall-cone penetrometer has been used to measure the evolution of the static yield stress over  
175 a certain period of time, as per the European standard "NF EN ISO 17892-6" [60]. Hereby, a 30°  
176 steel cone having a smooth surface has been used. 100 g further added to the system to ensure a  
177 significant penetration of the cone in the material [57].

178 The material was put in a circular steel container having a diameter of 30 cm and a depth of 5  
179 cm. The container was then put over a jolting table for 30 shocks to ensure a proper filling, and  
180 to remove any entrapped air bubbles. The surface of the container was gently sawn, and the  
181 excessive materials were cut off. The material was then left at rest for 120 sec. Once done, the tip  
182 of the cone was placed at the surface of the material, then it was released to fall under its own  
183 weight for 5 sec  $\pm$  1 sec, and the penetration depth " $h$ " was recorded. This procedure was  
184 repeated every 150 sec over a time span of 1320 sec (22 min). 5 cm were left between a  
185 penetration and another. Besides, the measurements were repeated three times, each on a  
186 different batch.

187 The static yield stress was derived from the penetration depth of the cone, and it was calculated  
188 using Eq. 1. In this equation, " $\tau$ " corresponds to the calculated yield stress (Pa), " $F$ " represents  
189 the force generated by the mass of the cone (N), " $h$ " is the penetration depth (mm), and " $\Theta$ " is  
190 the angle of the cone used (degrees).

191 
$$\tau = \frac{F \cos\theta^2}{\pi h^2 \tan\theta} [61] \text{ (Eq. 1)}$$

192 The linear model proposed by Roussel et al. [62] was adopted. However for this research, the  
193 initial yield stress " $\tau_{0,0}$ " at  $t=0$  sec was neglected because it has an insignificant magnitude  
194 relative to that developed when the mix is at rest. In fact, the total yield stress was presented in a  
195 simplified form following Eq. 2.

196 
$$\tau_{0(t)} = A_{\text{thix}} t [62] \text{ (Eq. 4)}$$

## 197 2.2- Specimens preparation for the submersion in sulfuric acid solutions

### 198 2.2.1- Mixing procedure

199 A uniform mixing procedure was adopted for the production of all samples from different mixes.  
200 It was always done at room temperature ( $\approx 22^\circ\text{C} \pm 2^\circ\text{C}$ ) to minimize the difference between  
201 batches. A DITO-SAMA 80 liters BMXE80 mixer was used. First, all solid ingredients were dry  
202 mixed for about 2 min at a low speed (20 RPM). Then after, water and HRWR were added  
203 gradually. After adding all liquids, the mixing speed was progressively increased to 100 RPM.  
204 The overall mixing process took around 10 min. During the mixing time, the walls of the mixer's  
205 bowl were scrapped using a large spatula to ensure that all materials were properly mixed. After  
206 finishing, the material was collected and directly placed inside the printer's pump.

### 207 2.2.2-Samples manufacturing

208 Two different sample categories were made for each mix composition. The first category  
209 included casted samples, taken as references. The second category included printed samples.  
210 First, the reference samples were casted inside  $4 \times 4 \times 16$  cm molds, in a single pour, without  
211 external vibration. This is to simulate the bulk material of each printed layer which can never be  
212 vibrated. Second, printed samples were done using an automated 3-axis gantry printer having a  
213 circular nozzle of 1.9 cm diameter (Fig. 2). Hence, the difference in the production of reference  
214 samples is the absence of multiple layers and pumping pressure.

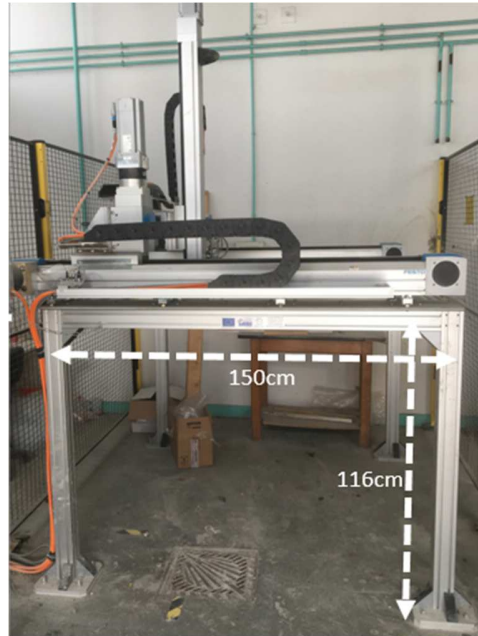


Figure 2: 3-axis gantry printer

215  
216

217 The standoff distance of the nozzle was fixed to 1 cm, in order to obtain a 1 cm thick layers.  
 218 Moreover, the printing speed was set to 6.4 cm/sec, and it was adjusted in a way to print a layer  
 219 having a width ranging between 5 and 5.5 cm. Indeed, in this case the printed layers were  
 220 compressed one on top of the other because of the pumping pressure exerted during printing that  
 221 allows for the material to spreads off and produce a layer of 5 cm out a 1.9 cm circular nozzle.  
 222 Fig. 3 shows a printed sample of each mix. All samples made out of the same mix have the same  
 223 number of superposed layers. It must be mentioned that, the layers were printed successively  
 224 with a time gap of 15 sec, corresponding to the applied printing speed (No additional time gap  
 225 has been intentionally added). After finishing, the samples were directly cut down (when the  
 226 material is still in its fresh state). All samples were left to cure at room temperature ( $\approx 22^{\circ}\text{C} \pm 2^{\circ}$   
 227 C) during the first 24 h.



Mix A

Mix B

Mix C

228  
229

Figure 3: Printed sample of each mix

230 After 24 h, non-printed samples were de-molded and kept at 100% RH at a temperature  $\approx 20 \pm 2^{\circ}$   
 231 C for 38 days. Then after, all printed and non-printed samples were cut down properly using a  
 232 cord saw with water discharge to make  $4 \times 4 \times 2$  cm specimens (Fig. 4). At the end, all samples  
 233 were placed inside the oven for 6 days at  $50^{\circ}\text{C}$  to cease the hydration process.

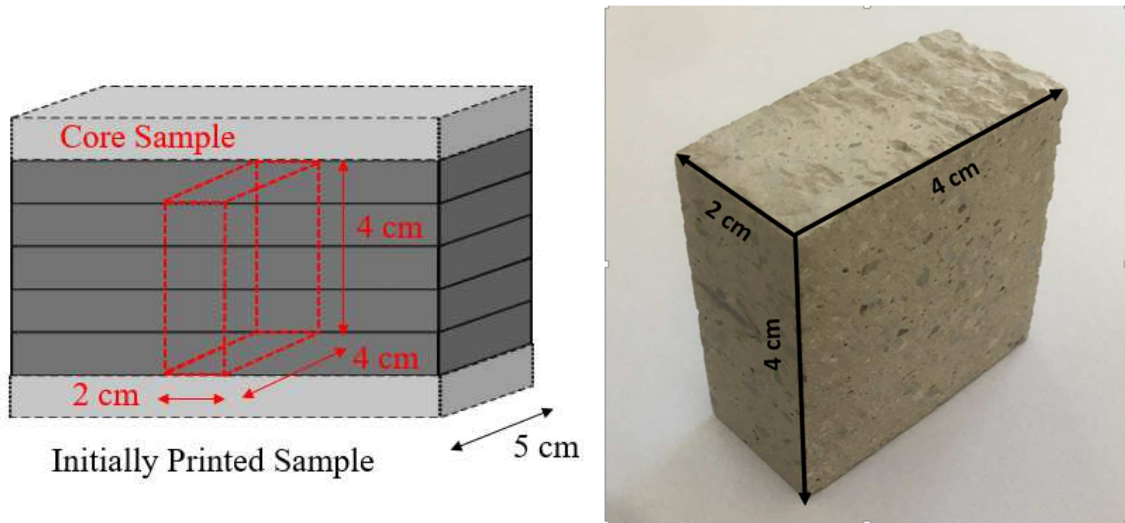


Figure 4: Testing sample

234

235

236 It should be noted here that printed samples were initially cut down, and only the core samples  
 237 were subjected to acidic environment, to qualify exclusively the interface properties resulting  
 238 from the layers superposition. In other words, this is done to eliminate first the vulnerable  
 239 interfaces between consecutive layers generating concentration ports for acid ingress. Second, to  
 240 guarantee that micro-cracks no longer exist at the surfaces. This issue must be taken seriously,  
 241 because in 3D printing, concrete elements are more susceptible to micro-cracks caused by the  
 242 plastic shrinkage and temperature strains, due to the absence of formworks.

### 243 2.3- Sulfuric acid exposure

244 The Sulfuric acid ( $H_2SO_4$ ) used has an initial concentration of 98%. Two samples of each  
 245 production method and mix design were submerged in a bath of 1% and 3% sulfuric acid  
 246 solution separately (the choice of these concentrations was based on the literature [50], [63]).  
 247 The volume of the solution was equal to four times the volume of submerged solid, as suggested  
 248 by the standard test method for mortars exposed to sulfate attack (ASTM C1012/C1012M – 18b)  
 249 [64]. The specimens were laid on plastic supports, inside hermetic plastic containers to prevent  
 250 any evaporation (Fig. 5). The storage temperature was maintained at  $22 \pm 2^\circ C$ , and the solution  
 251 was renewed at 3, 7, 14, 21, 28 and 42 days.



Figure 5: Specimens of the same mix placed inside a plastic container

252

253

#### 254 2.4- Macroscopic characterization

255 All samples were gently cleaned using a brush and dried using paper towels before each solution  
256 renewal. This process was done to remove poorly adhered corroded material. Then after, a  
257 visual assessment of the corroded samples caused by the damage progression on the concrete  
258 elements surfaces was carried out, and the mass loss of each sample was recorded, during each  
259 solution renewal.

#### 260 2.5- Microscopic characterization

##### 261 2.5.1- Mercury Intrusion Porosimetry (MIP)

262 The description of the pore structure and their distribution play an important role when studying  
263 the durability of cementitious materials. In general, these pores are classified into macro-pores,  
264 capillary pores, and gel pores. However, there is no common agreement on the ranges describing  
265 the boundaries of each pore size [65]. In addition, until now there is no test or method that could  
266 measure the entire pore structure at once [46]. However, in this study it was decided to measure  
267 the pore size distribution using the Mercury Intrusion Porosimetry (MIP) for all non-degraded  
268 samples.

269 To study the porosity of all samples, printed and non-printed specimens having the dimensions  
270 of 1×1×1 cm were obtained from the core of the original ones. These specimens were carefully  
271 cut using a very precise cord saw with water discharge. It should be mentioned that for the  
272 printed samples, the specimens were carefully taken in a way to insure the presence of an inter-  
273 layer inside of it. The masses of the tested samples ranged between 2.5 g and 3 g.

##### 274 2.5.1- Scanning Electron Microscopy (SEM)

275 The Scanning Electron Microscopy (SEM) was used to characterize and visualize the inside of  
276 the degraded and non-degraded samples, and to explore the microstructural characteristics of all  
277 specimens. Herein, only degraded samples that were submerged in a solution of 1% acidic

278 concentration were analyzed, because those who were attacked by a solution containing 3% acid  
279 were severely deteriorated.

280 The tested samples were cut off from the original ones using a cord saw with water discharge.  
281 The size of each sample to be visualized was equal to 1.5×1.5 cm×“thickness of the sample” (the  
282 thickness of non-degraded samples is equal to 2 cm, whereas the thickness of degraded samples  
283 ranges between 1.7 cm and 1.9 cm depending on the degree of corrosion). Then after, these  
284 samples were impregnated with a low viscosity epoxy resin under vacuum, and cured for 24 h  
285 until the resin is fully hardened. Precisely, samples were embedded in resin (H2020, Huntsman)  
286 under vacuum (pressure 100 – 200 mbar). After the resin hardens, the thin excess at the sample’s  
287 surface were removed carefully using 80 grit diamond discs (Struers MD System) and grounded  
288 using successive decreasing abrasive sizes 220 and 500 for around 5 sec and 30 sec respectively  
289 with a 25 N load on MD discs rotating at 150 rpm. The 1200 grit stage was carried out under the  
290 same conditions for around 1 min. A manual lapping using 800 grit powder SiC mixed with  
291 ethanol was carried out on a glass plate. Then after, fine polishing was carried out on woven  
292 discs (MD Dac) with diamond pastes. Herein, samples were grounded first using 6 μm diamond  
293 paste for no more than 5 min at 30 rpm. Afterwards, samples were grounded using 3 μm  
294 diamond paste at 40 rpm for 3 min. At the end, the samples were grounded using 1 μm diamond  
295 paste at 60 rpm for 1.5 min. Between each step, water free lubricants was used (Struers DP  
296 Brown) to carry out cleaning in depth with ethanol, soft brushes and cotton.

297 Fig. 6(a) shows the tested specimen extracted out of the original sample, and Fig. 6(b) shows a  
298 front view of one cut side, as well as the observation directions. All observations were conducted  
299 over the cut surfaces to visualize the inside of the element and not the degraded surfaces. For the  
300 non-printed samples (whether degraded or not), a random cut side was observed by the SEM  
301 since there is no layers to be perceived. However in this study, special care was taken to  
302 visualize the internal structure of the printed samples in order to locate the inter-layer, if any is  
303 still existing after the complete setting and hardening of the material. For the non-degraded  
304 printed samples, the layers direction was known, and the SEM observation was carried over the  
305 correct cut side. Though, because of the complete surface deterioration of the degraded printed  
306 samples subject to sulfuric acid attack, all signs indicating the layers direction were ruined.  
307 Therefore, horizontal and vertical observations were done over both cut sides of the same  
308 sample.

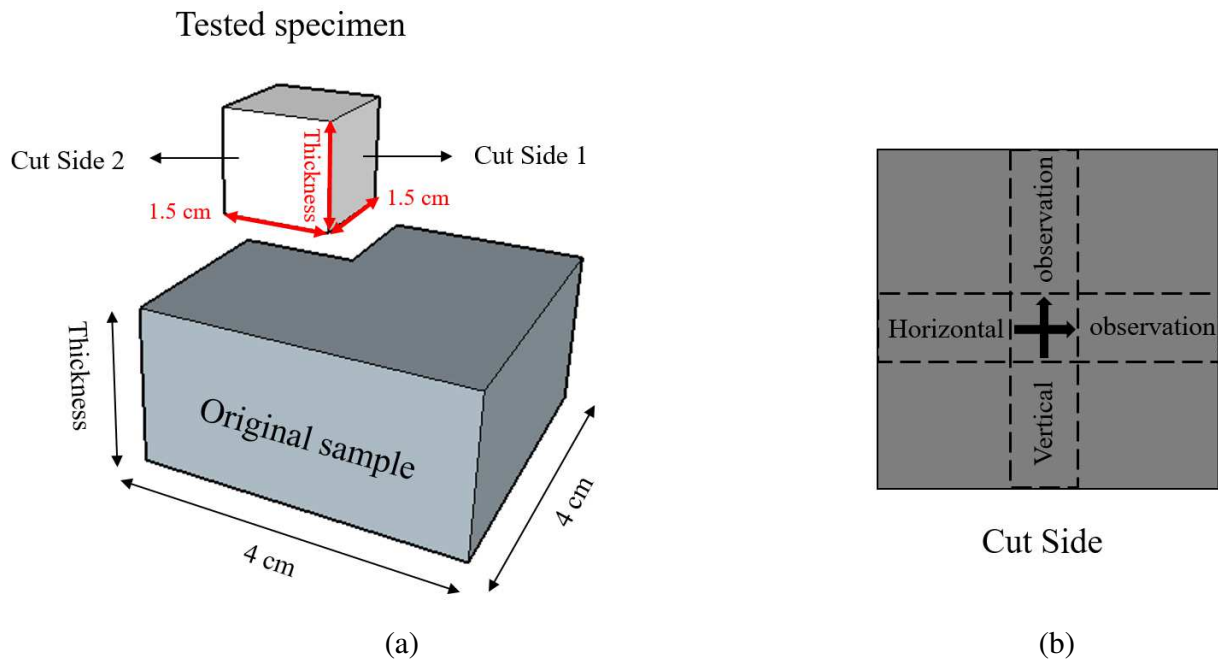


Figure 6: Schematic illustration of SEM samples

### 3- Results and discussion

#### 3.1- Mechanical performance of mortars

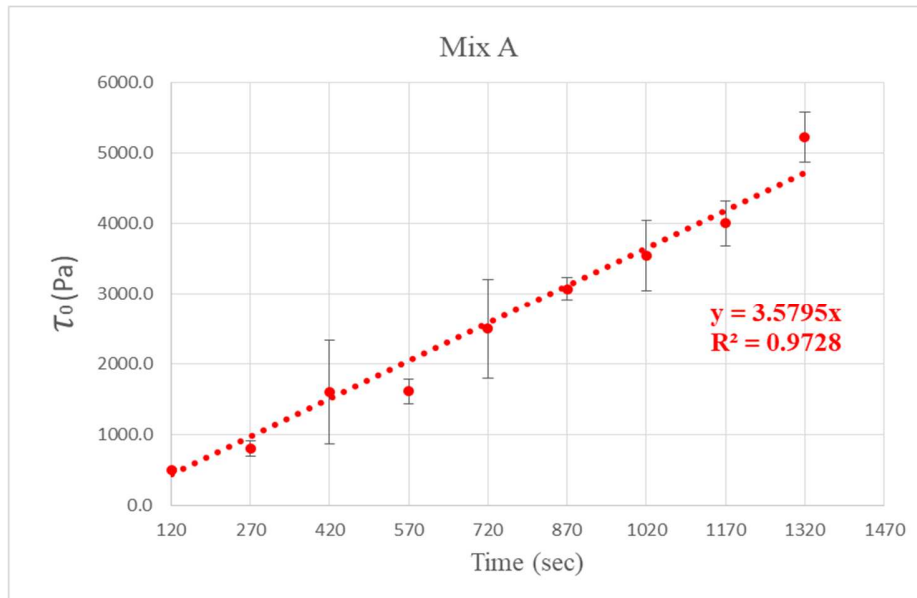
Mix A, Mix B, and Mix C gave a compressive strength equal to 48 MPa, 57 MPa, and 73 MPa respectively. Herein, the resistance attained by Mix C was the highest among other mixes, because it has the lowest water to cement ratio. However, it was anticipated that Mix A yields a higher strength than Mix B because it has a lower limestone filler content. This is further detailed by Baz et al. [57].

#### 3.2- Fall-cone and thixotropy results

Fig. 7, Fig. 8 and Fig. 9 show the yield stress evolution in function of time for Mix A, Mix B, and Mix C with their standard deviations respectively. These results pointed out that for all mixes the yield stress is almost linear during the first 1320 sec. For that given period, Roussel's model predicted a reasonable structural build-up rate of the material, and this was further confirmed by the corresponding correlation factors ( $R^2$ ) for each mix. Though, the equivalent thixotropic index " $A_{thix}$ " describing the slope of the curves was equal to 2.85, 5.17, and 17.23 for Mix A, Mix B, and Mix C respectively. Hence, these mixes representing different  $A_{thix}$  values cover a wide range of materials having various rheological properties used for 3D printing applications. Therefore, the findings of this research could be applied over a broader range of printable material.

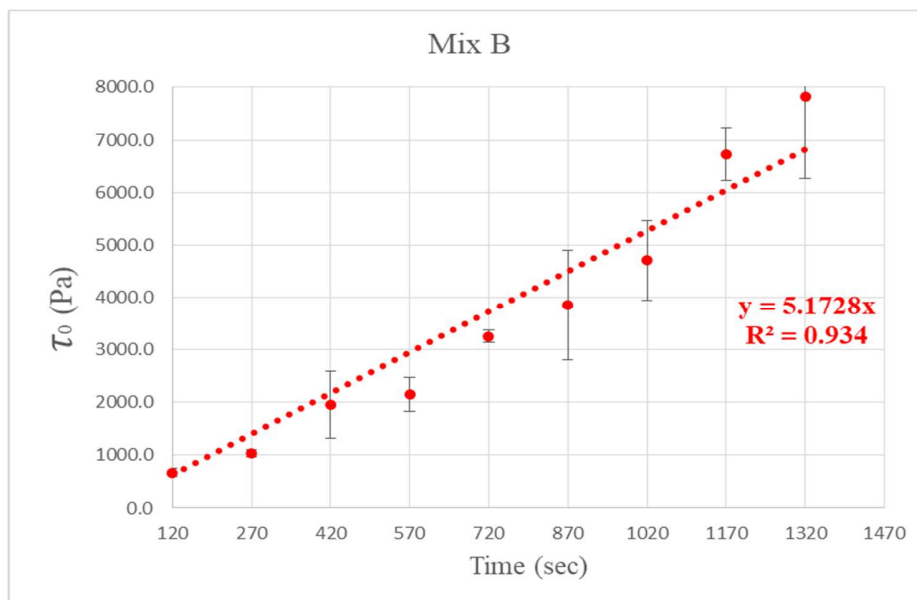
However, it should be mentioned that the time course over which the yield stress evolution of Mix C was limited to 870 sec, just to keep on using the simplified linear model proposed by Roussel et al. [62] for the analysis of results. Precisely, the variation of the yield stress was not linear when going through the entire time scale (up to 1320 sec), and the exponential model

334 proposed by Perrot et al. [66] was more representative, because it gave a higher correlation factor  
 335 ( $R^2$ ). Therefore, it was decided to divide the growth rate of the yield stress into two stages. The  
 336 first stage defined between 120 sec and 870 sec, presented a slow and linear increase of the yield  
 337 stress. The second stage presented a fast development of the yield stress until the end of the  
 338 testing time. That being the case, the results were limited to the first stage.



339  
 340

Figure 7: Yield stress variation in function of time for Mix A



341  
 342

Figure 8: Yield stress variation in function of time for Mix B

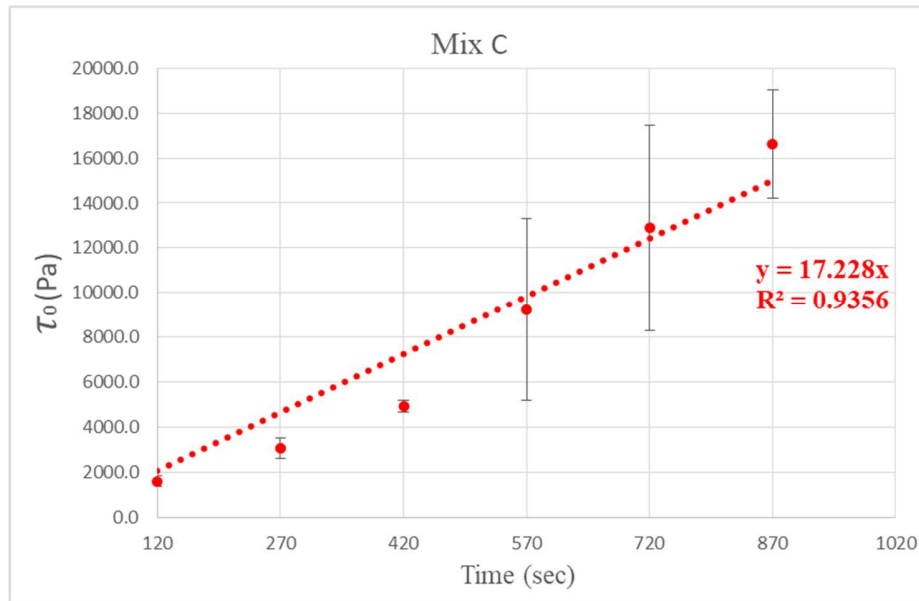


Figure 9: Yield stress variation in function of time for Mix C

343

344

### 345 3.3- Macroscopic analysis and results

#### 346 3.3.1- Shape deterioration and visual assessment

347 Fig. 10 and Fig. 11 visually show the progression of damage on the surface of concrete samples  
 348 exposed to a 3% and 1% acidic solution at different ages respectively. It can be clearly seen that  
 349 after 3 days of continuous immersion, printed and non-printed concrete samples from all mixes  
 350 started to show a mild corrosion, characterized by a slight spoiling of the cement paste. However,  
 351 as the immersion period increases, the material's loss became greater and more significant,  
 352 especially with the higher concentration of sulfuric acid in the solution. Thus, after 56 days of  
 353 immersion the samples presented a very porous surface structures, in addition to a more  
 354 significant corrosion and spoiling of the paste leading to an irregular shape and smaller size of  
 355 the specimens. Over and above, it can be noticed that the printed and non-printed samples of all  
 356 mixes were in general equally deteriorated for each submersion condition. Herein, the printed  
 357 and non-printed samples showed a thinner section with much more exposed aggregates when  
 358 compared to shorter immersion periods. Though, it must be mentioned that for the case of all  
 359 printed samples of all mixes, no inter-layer was observed and no cracks appeared at that level.

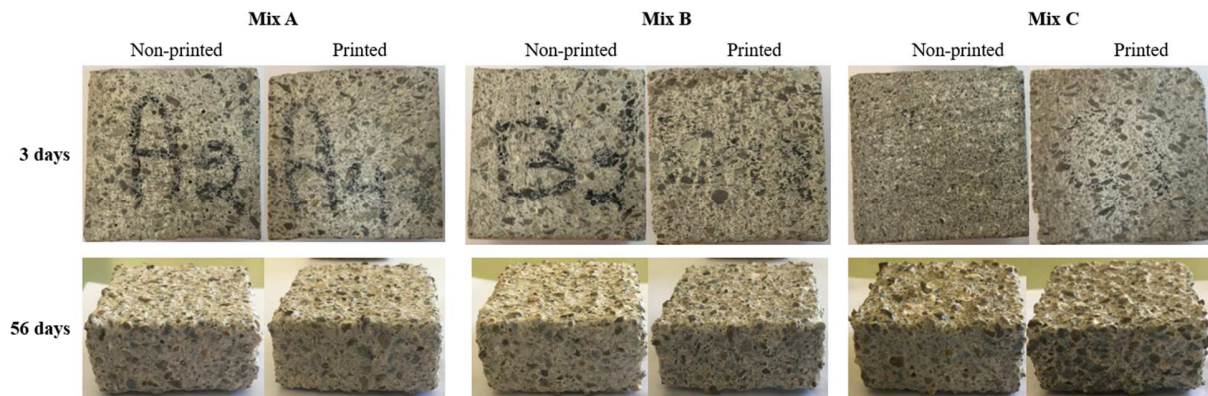


Figure 10: Progressive damage of printed and non-printed samples in 1% acidic solution

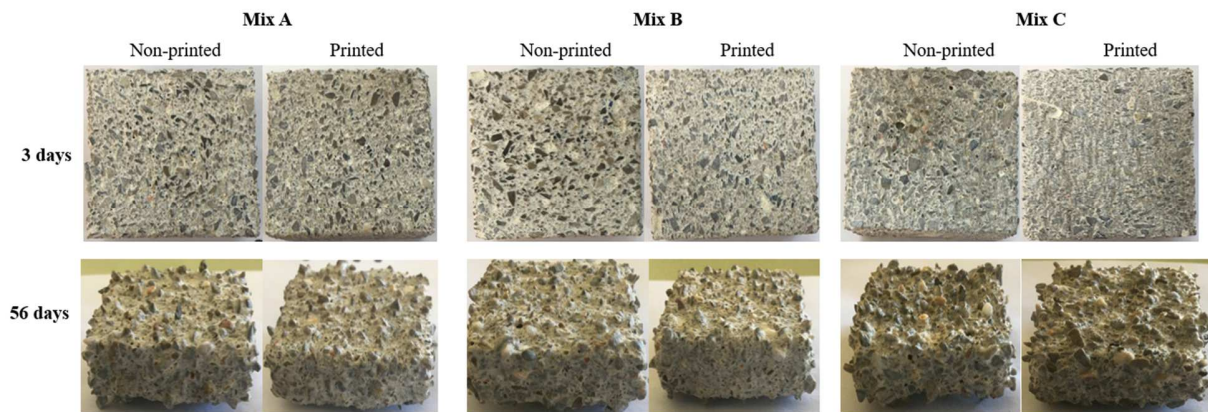


Figure 1: Progressive damage of printed and non-printed samples in 3% acidic solution

### 3.3.2- Mass loss

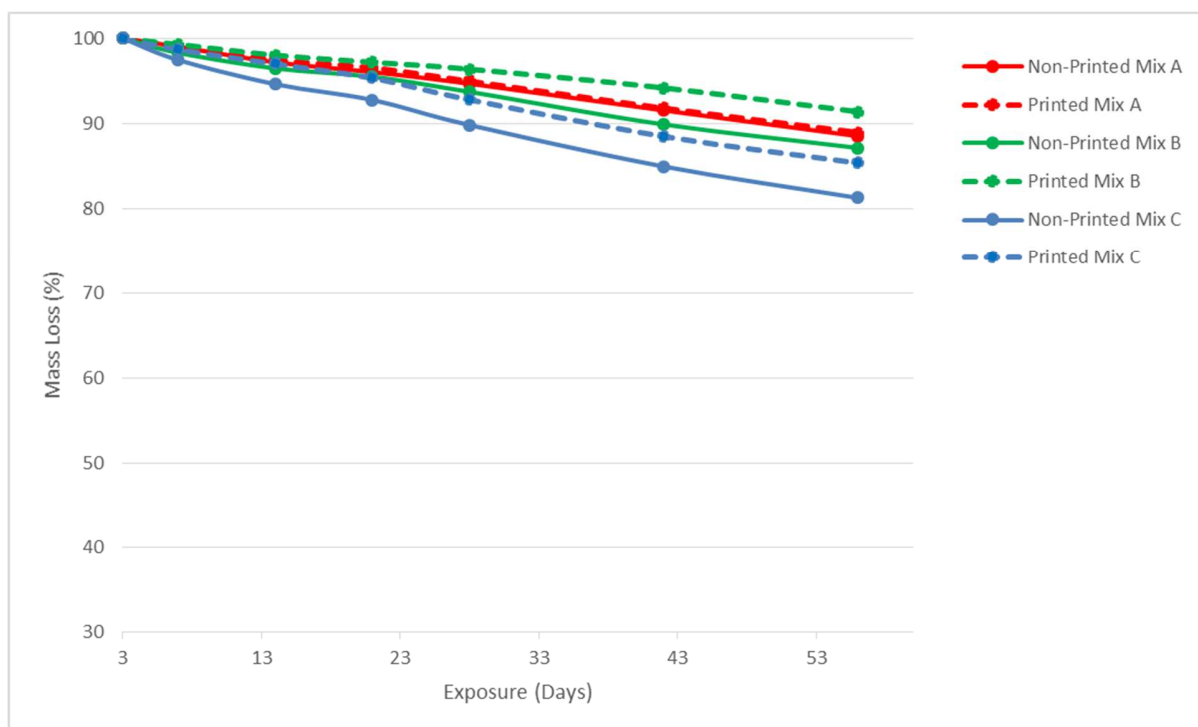
In principal, sulfuric acid reacts with the hydration product of cement in concrete, and produce gypsum. The formation of gypsum increases the volume of concrete, and reacts then after with calcium aluminate ( $C_3A$ ) to produce ettringite. The volume of ettringite formed inside the concrete element causes inner pressure, leading to the creation of cracks, and therefore acid infiltration to the inside of the elements through the cracks, causing concrete spalling and mass loss [63].

Fig. 12 (a) and Fig. 12 (b) show the change in mass relative to the initial weight of the specimens measured after 3 days of immersion for all samples when subjected to 1% and 3% acidic solutions respectively. A continuous decrease of mass in all samples in different conditions is always observed for all mixes. However, the mass loss of the samples submerged in sulfuric acid having a concentration of 1% was much lower than the samples put in a solution having a concentration of 3%. Yet, the rate of decrease in non-printed samples was systematically higher than that of the printed ones.

In particular, Mix C showed the highest mass loss among other mixes. Though, it is not a matter of higher  $A_{thix}$  value, instead, it is majorly related to the water to cement ratio. Thus, as a matter of fact, this variance was not obvious between Mix A and Mix B because they both have the

379 same water content, but only different limestone filler content. Particularly, previous studies  
380 found that a decrease in the water to cement ratio results in an increase of mass loss [48]. This  
381 happens even if a mix having a lower water to cement ratio is relatively denser and has fewer  
382 pores. However, knowing that a denser structure better prevents the absorption of sulfuric acid  
383 toward the inside of the sample, but still it presents an abundant amount of hydrates. Thus, as  
384 time progress the acid reacts with the cement paste over a larger concrete surface causing much  
385 more significant deterioration [48].

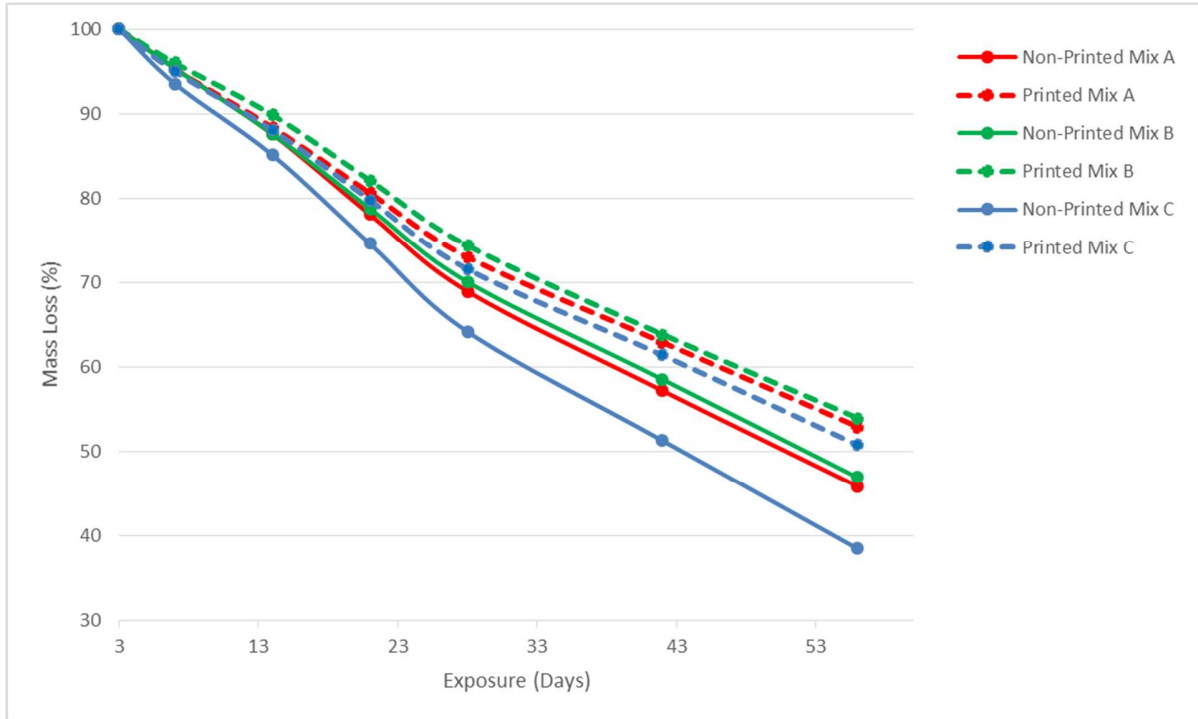
386 As for the current study, it can be said that 3D printed elements were strong enough to resist  
387 further deterioration and mass loss. Hence, this gives an indication that the inter-layers did not  
388 allow the solution to further penetrate inside the element, and therefore to react and ruin a larger  
389 surface of the specimen.



390

391

(a)



(b)

Figure 12: Mass loss of printed and non-printed concrete samples exposed to a solution containing (a) 1% and (b) 3% sulfuric acid

392

393

394

395

### 396 3.4- Microscopic analysis and results

#### 397 3.4.1- Mercury Intrusion Porosimetry results

398 Table 3 shows the total porosity for all mixes and conditions. The total porosities of printed and  
 399 non-printed samples, for all mixes were comparable. The non-printed samples made of Mix A,  
 400 Mix B, and Mix C, had a porosity equal to 13.58%, 13.74%, and 11.23% respectively.  
 401 Alongside, the total porosity of the printed samples of, Mix A was equal to 13.11%, Mix B equal  
 402 to 12.89%, and Mix C equal to 11.67%. However, the distribution of pores differed largely  
 403 between printed and non-printed specimens, as can be observed in Fig. 13-15. Figures 13(a),  
 404 14(a), 15(a) show the cumulative pores volume between 1  $\mu\text{m}$  and 0.01  $\mu\text{m}$ , whereas Figures  
 405 13(b), 14(b), 15(b) show the total amount of pores between 1  $\mu\text{m}$  and 0.1  $\mu\text{m}$ , and less than 0.1  
 406  $\mu\text{m}$  independently.

407 Table 3: Total Porosity

	Mix A		Mix B		Mix C	
	Non-printed	Printed	Non-printed	Printed	Non-printed	Printed
<b>Total Porosity (%)</b>	13.58	13.11	13.74	12.89	11.23	11.67

408

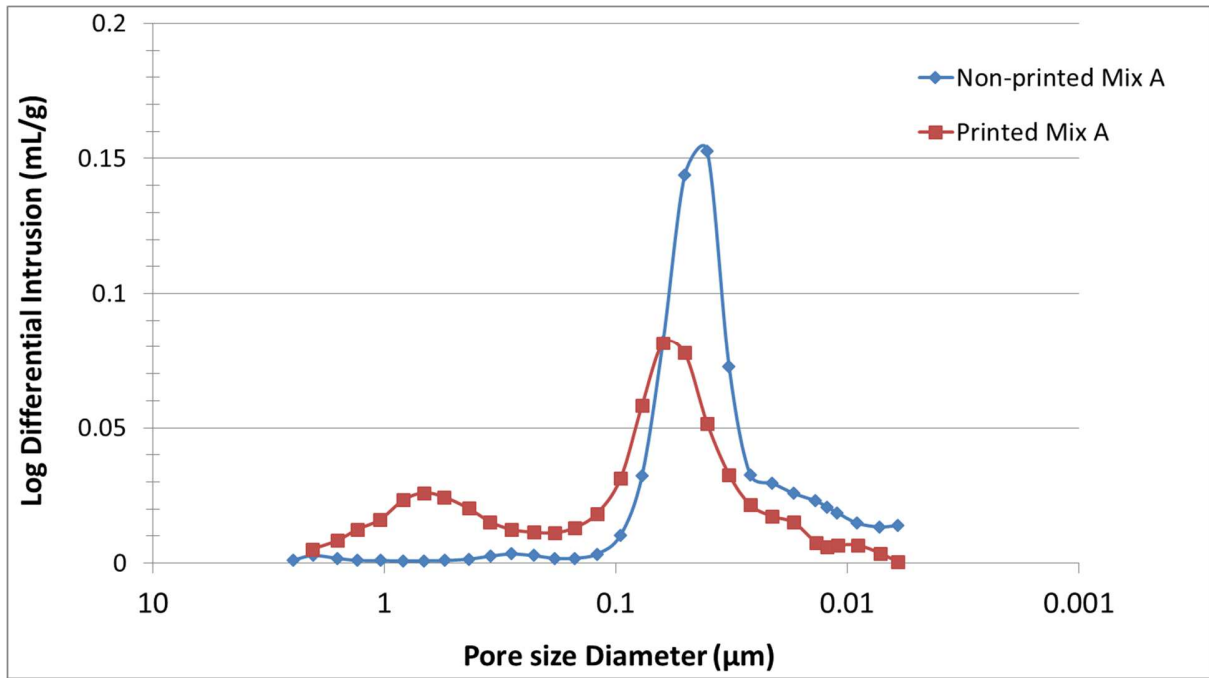
409 Despite the variance in the pore size distribution found among mixes between non-printed and  
 410 printed samples, the target of this particular study is to provide a comparison between both types

411 of samples within each mix individually. Hence, when comparing the results of the non-printed  
412 specimens to those of the printed ones in all mixes, it can be clearly seen that the non-printed  
413 samples show a much higher concentration of pores having diameters less than 0.1  $\mu\text{m}$ . On the  
414 other hand, the results of printed samples of all mixes indicated the presence of a larger  
415 concentration of pores ranging between 1  $\mu\text{m}$  and 0.1  $\mu\text{m}$ , which are negligible in the non-printed  
416 ones.

417 Based on the results of the MIP analysis, exposing the differences in the pore size distribution  
418 between printed or non-printed samples while having almost the same total porosity; this  
419 difference can be attributed to the external pressure exerted over the material when being printed  
420 [67]. As previously mentioned in section 2.2.2, non-printed samples were not vibrated on  
421 purpose, to get closer as much as possible of the material's internal structure inside of each  
422 printed layer that is not subject to any type of vibration. Thus, the only difference between the  
423 two production methods is the pumping pressure put over the deposited layers. Yet, the extruded  
424 material is subject to high shearing stresses, causing a deflocculation of the material's internal  
425 structure, leading to a better rearrangement of the small particles including cement grains. Hence,  
426 this fact decreases the concentration of pores having a diameter smaller than 0.1  $\mu\text{m}$ .

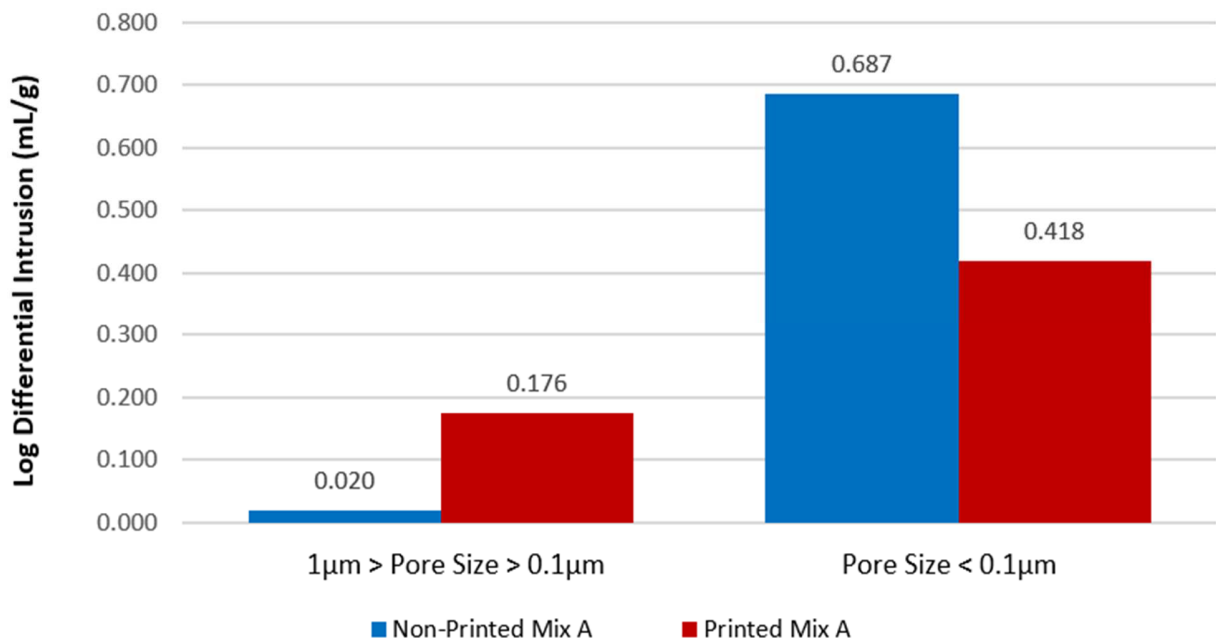
427 Few studies concerning the durability aspects and the effect of the pore size distribution were  
428 found in the literature, still no one provided a comparison between the different production  
429 methods (printed and non-printed). Schrofl et al. [68] discussed the increasing capillary water  
430 intake with respect to the increasing time gap between layers deposition. They found that a time  
431 gap up to 13 min was short enough to avoid preferential capillary suction at the inter-layer level.  
432 However, a time gap of 24 h would certainly give rise to quick capillary suction through the  
433 inter-faces because of the formation of more accessible pores. Similarly, Van der Putten et al.  
434 [69] found that no additional porosity is induced while not having additional time gap between  
435 layers deposition. However, a much denser matrix is formed due to the low porosity found in  
436 samples with no time gap, which in its turn is caused by the material's compaction performed by  
437 the layer being printed over the one underneath. Bran-Anleu et al. [70] investigated the chloride  
438 penetration in 3D printed specimens for different interval times, and found that the penetration  
439 rate is significantly higher for longer time gaps due to the formation of additional voids between  
440 superposed layers. Hence, these previous findings support the results of this research.

441



442  
443  
444

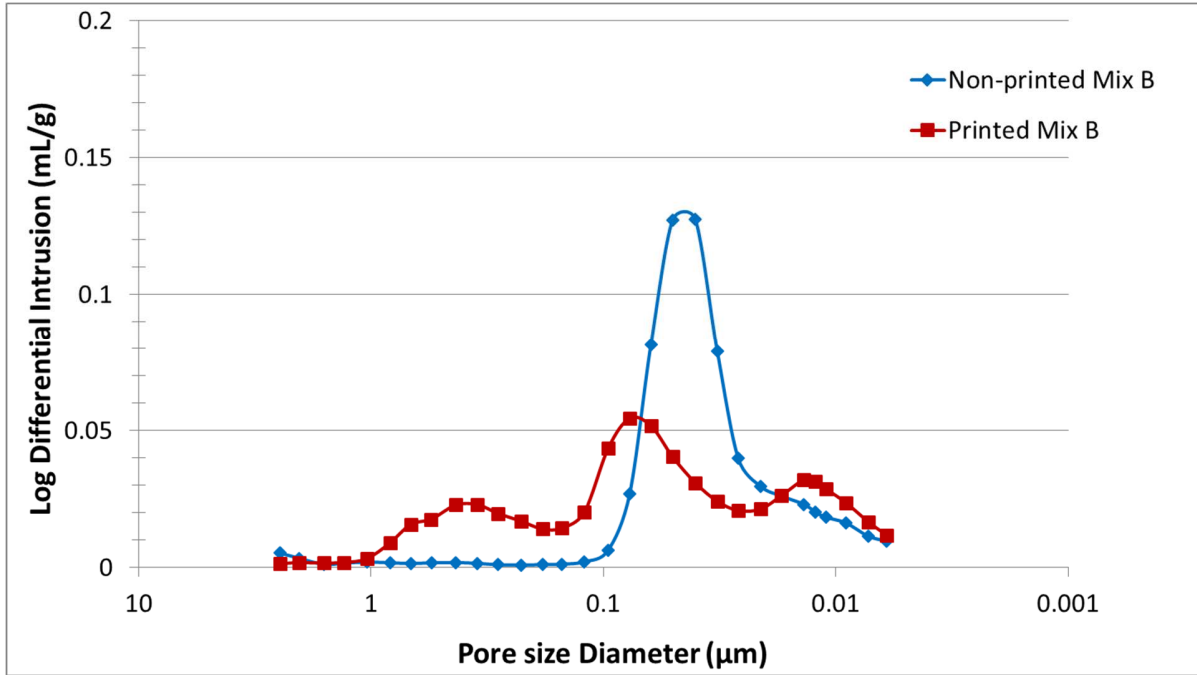
(a)



445  
446  
447

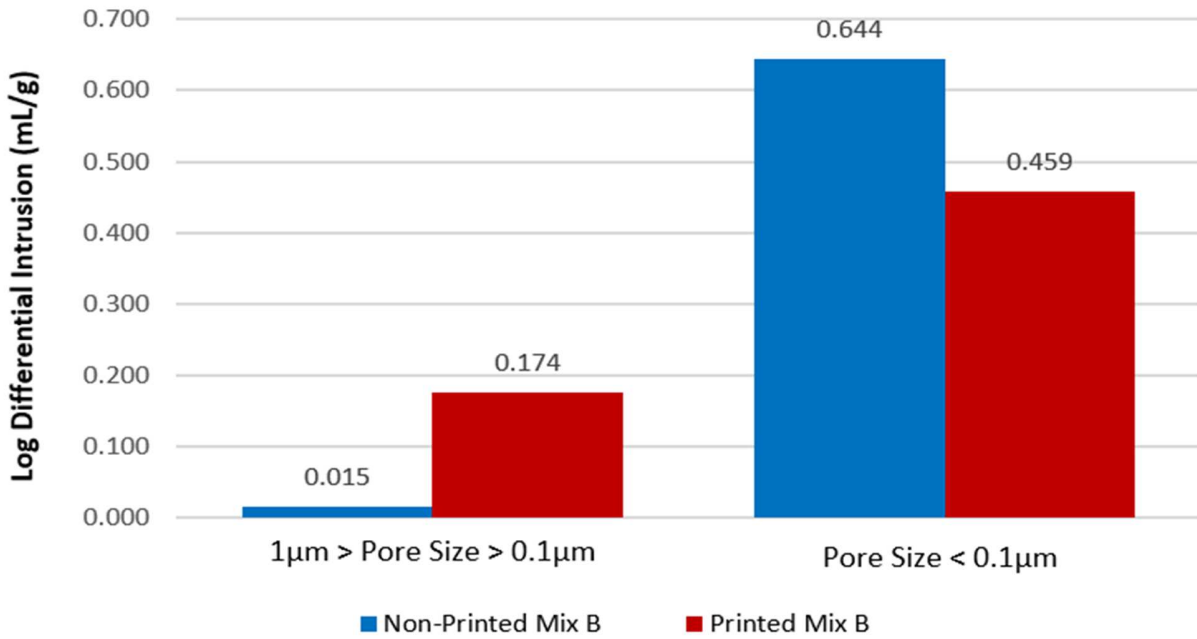
(b)

Figure 13: Pore size distribution of printed and non-printed elements Mix A



448  
449

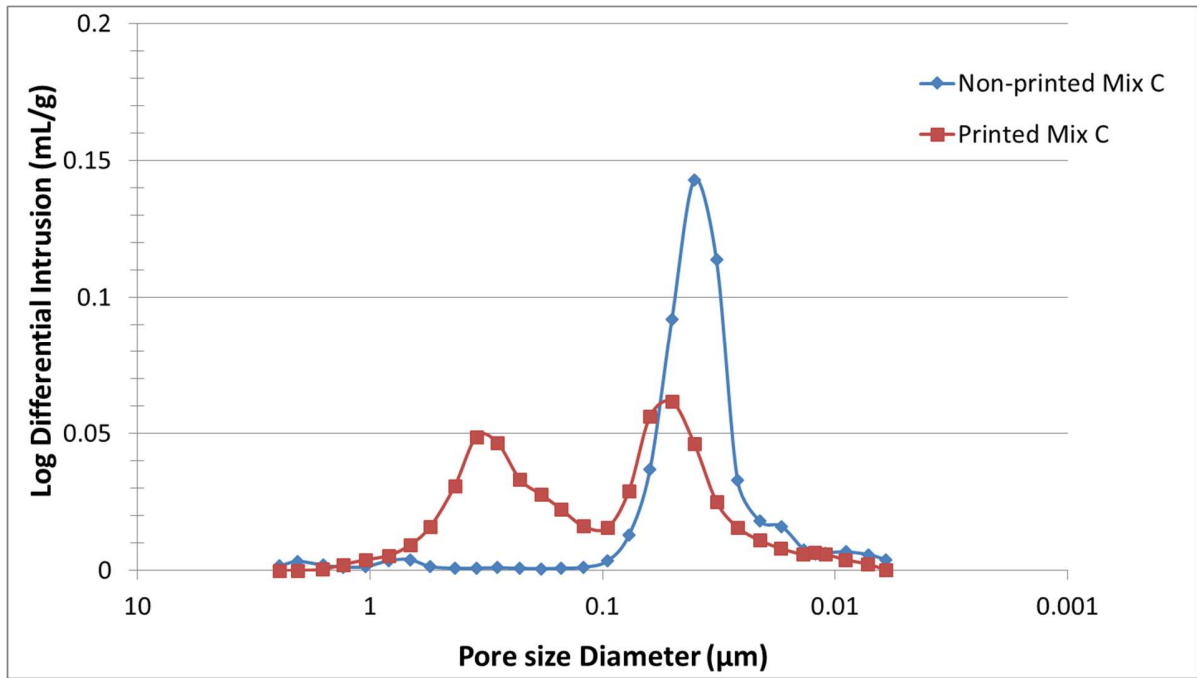
(a)



450  
451  
452

(b)

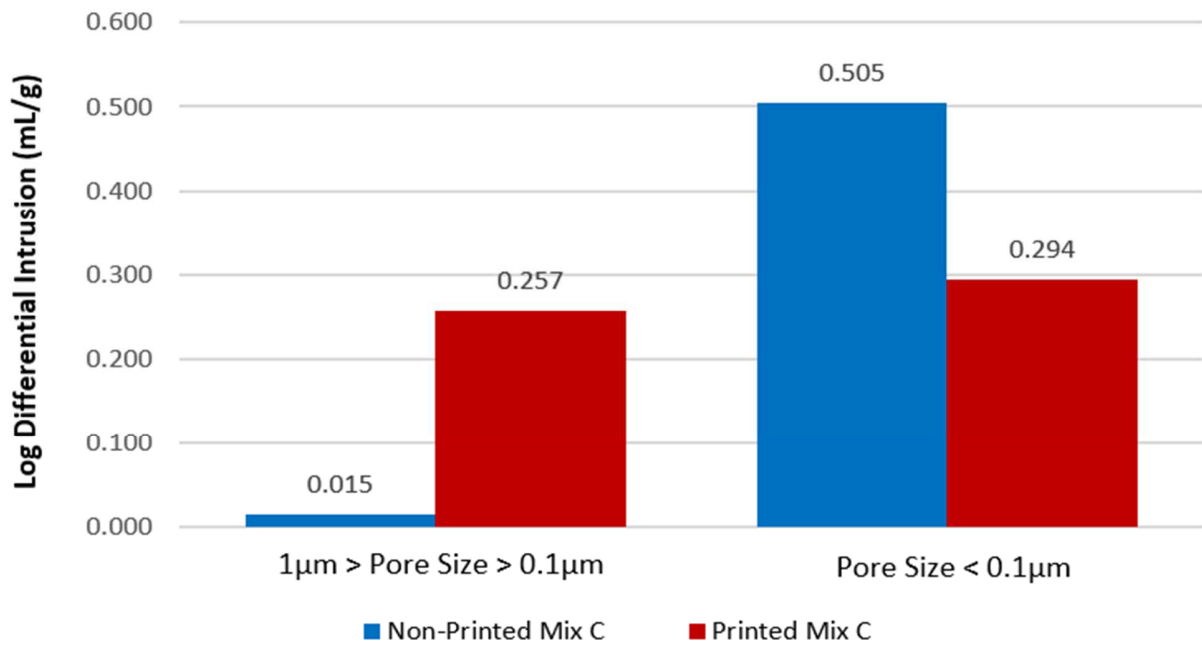
Figure 14: Pore size distribution of printed and non-printed elements *Mix B*



453

454

(a)



455

456

(b)

457

Figure 15: Pore size distribution of printed and non-printed elements Mix C

458 3.4.2- Scanning Electron Microscopy results

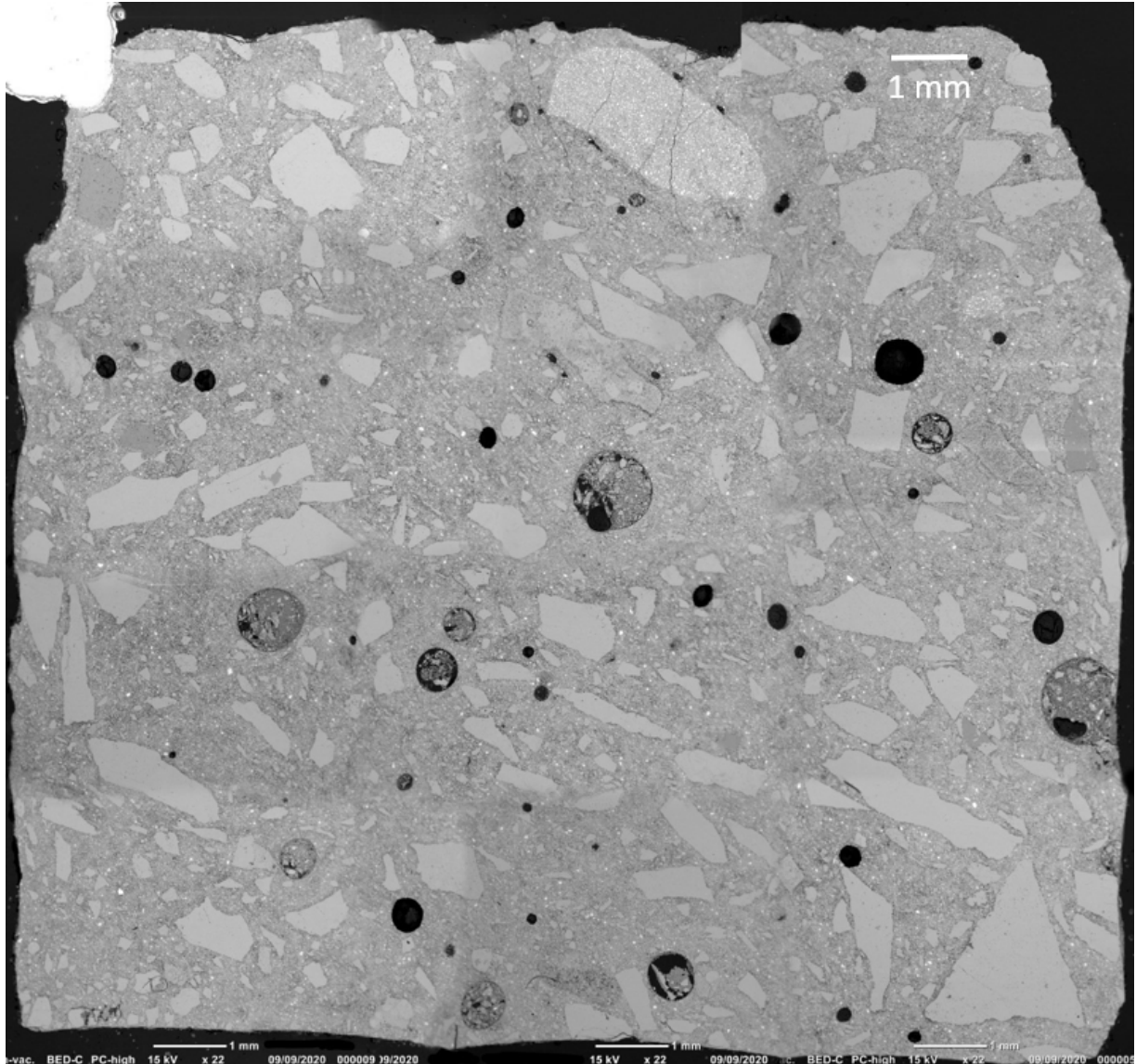
459 Based on the external appearance and shape of the printed elements shown in Fig. 3, it was  
 460 decided to start by visualizing the specimens of Mix A. The printed layers are much more

461 exposed than those of Mix B and Mix C. Therefore, it was presumed that if any inter-layer is to  
462 be identified, it has to be more visible in Mix A rather than other mixes.

463 Herein it should be noted that all presented figures are a collection of 38 independent SEM  
464 pictures that were organized and rearranged altogether to render a full image of the cut surface  
465 under display.

466 Fig. 16 shows the microstructure of a non-degraded and non-printed sample using Mix A,  
467 whereas Fig. 17 shows the microstructure of a non-degraded printed sample, at the cut side  
468 where the inter-layer must be located. It can be seen from Fig. 17 the presence of spherical pores  
469 of different volumes. This indicates that the larger pores are entrapped air bubbles, only caused  
470 by the production method, which did not use any vibration in this case. On the other hand, the  
471 majority of the pores in a printed sample (Fig. 17) have an irregular and deformed shape, unlike  
472 those found in the non-printed sample (Fig. 16). In fact, the void deformations in printed samples  
473 are caused by the external pressure applied on the material when being extruded. Besides, it can  
474 be also seen that the concentration of medium pores ( $1\mu\text{m} > \text{Pore size} > 0.1\mu\text{m}$ ) is higher than in  
475 the non-printed sample, and this is previously confirmed by the MIP results in section 3.4.1.

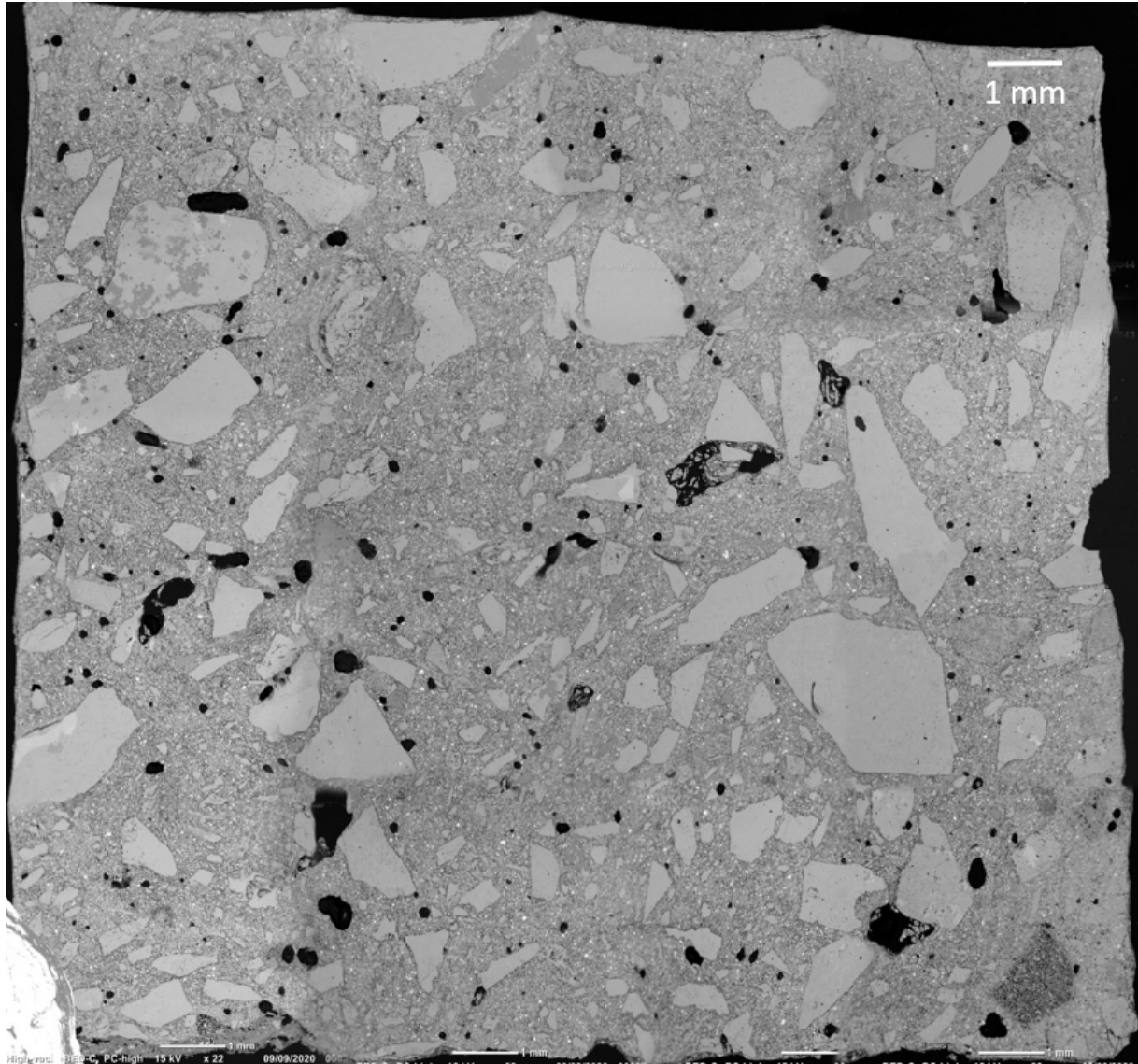
476 Above all, if we take a deeper look over Fig. 17, no inter-layers can be identified. The pores do  
477 not present a continuous pattern over the cut surface, neither in the horizontal nor the vertical  
478 directions. As well, no crack lines were recognized that can provide any information about a  
479 weak plane. Even more, it is worth mentioning that the printing direction did not dictated a  
480 certain orientation of the sand grains. In addition, there cannot be seen any thin strip of  
481 continuous cement paste which could unveil the contact plane between the subsequent layer and  
482 the upper one. This fact gives an indication that the superposed layers merged well, and the sand  
483 grain crossed the inter-layers. Hence, this might be due to the kinetic energy of the suspended  
484 sand particles owing to the pumping pressure.



485

486

Figure 16: Microstructure of the non-degraded / non-printed sample Mix A



487

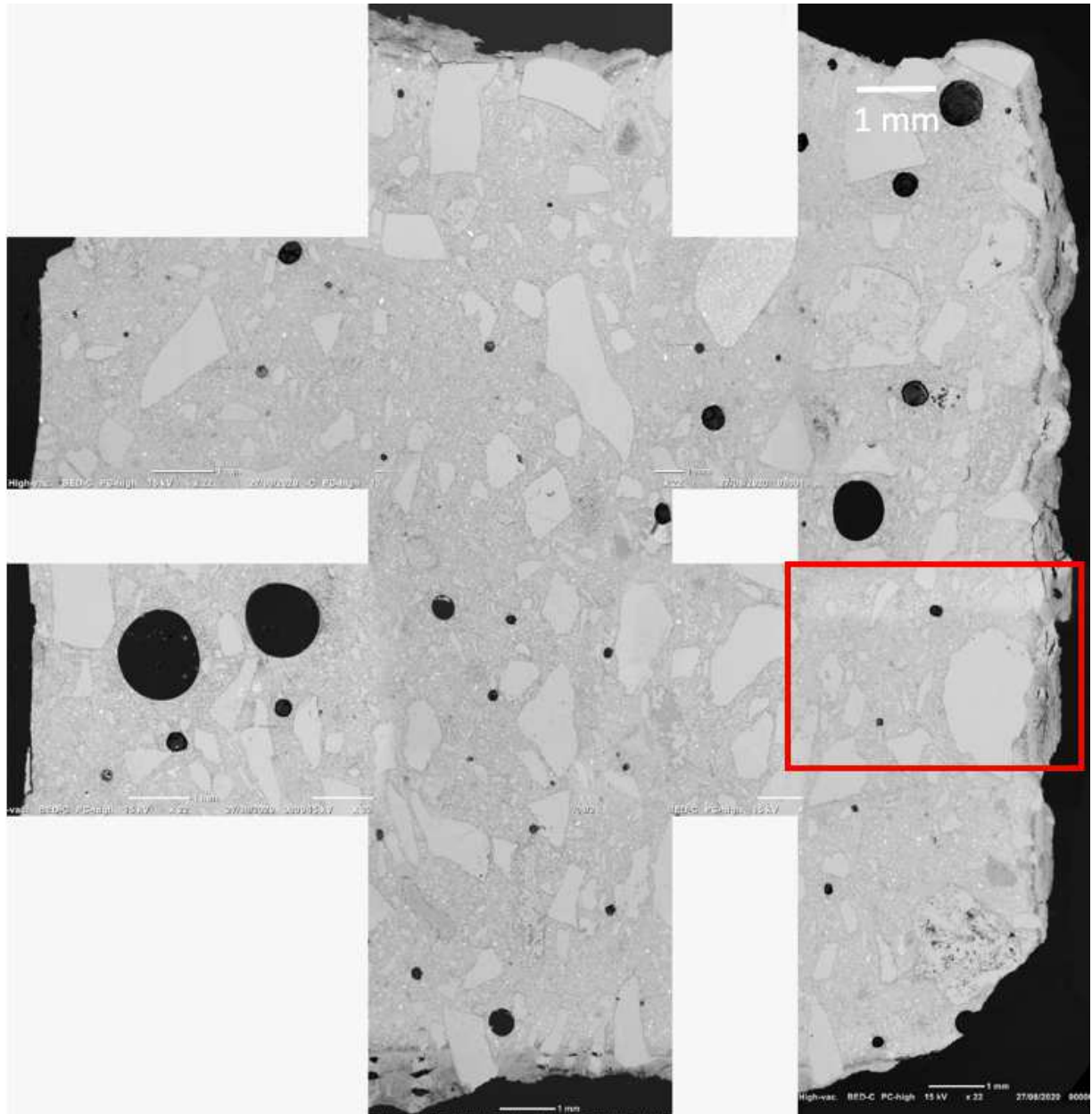
488

*Figure 17: Microstructure of the non-degraded / printed sample Mix A*

489 Concerning the degraded samples, Fig. 18 shows the microstructure of the non-printed sample of  
490 Mix A after 56 days of acid exposure. The same interpretation reported on the non-degraded  
491 sample of Fig. 15 applies over the degraded one. Except that, in the case of degraded sample, the  
492 outer surface in contact with the solution has been damaged, as well as the smallest pores located  
493 near the surfaces in contact with the surrounding environment and reached by the acid solution  
494 ingress, were closed due to the precipitation of gypsum (small white dots) caused by the sulfate  
495 contained in the sulfuric acid (Fig. 19).

496 Fig. 20 and Fig. 21 show the microstructure of cut side 1 and cut side 2 respectively of the tested  
497 specimen extracted from the degraded printed element after 56 days of acid exposure (the two  
498 sides were observed for the reason previously explained in section 2.5.1). Still, even in a  
499 degraded printed sample, the inter-layers are not spotted neither at cut side 1, nor at cut side 2.

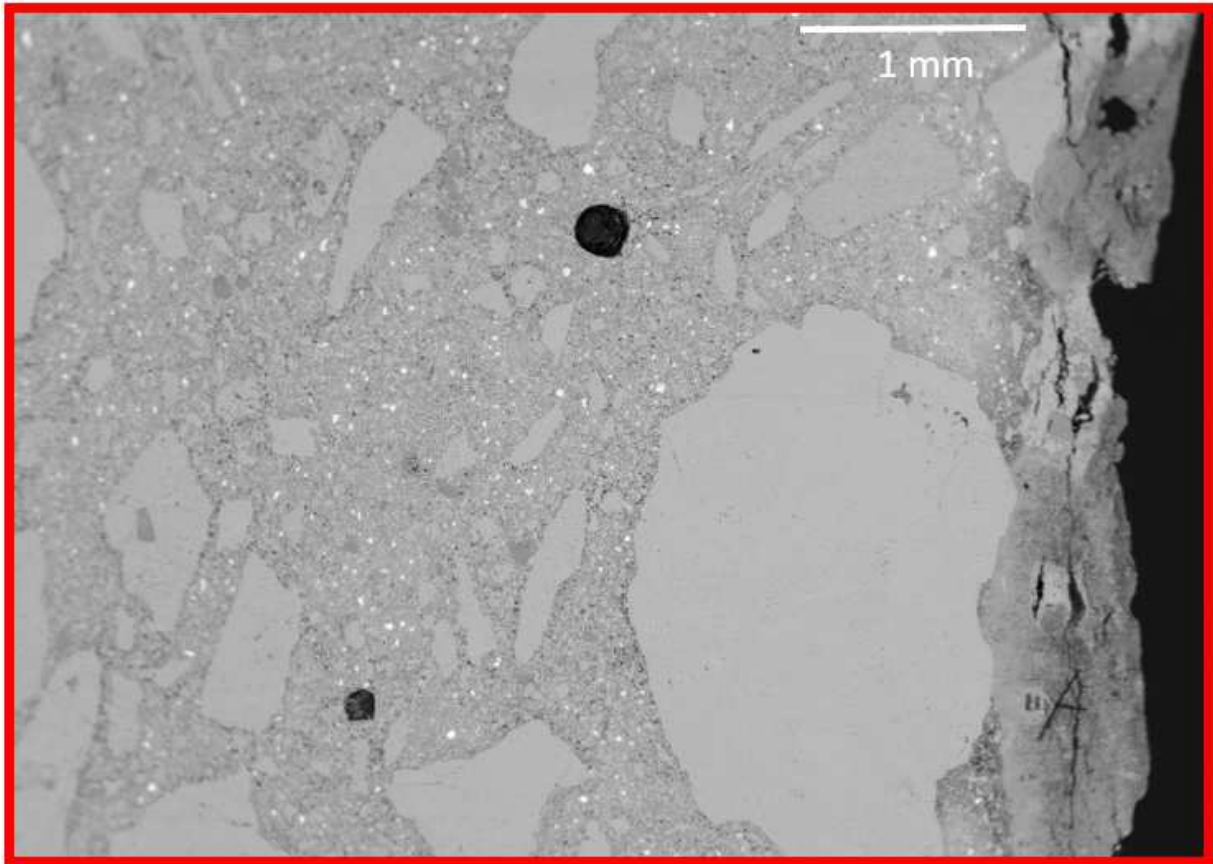
500 This fact confirms that the inter-layer are not weak planes that create a preferential path for the  
501 solution's ingress into the concrete element. Herein, it can be said that the printed element acted  
502 like a monolithic body, and had a homogeneous microstructure.



503

504

Figure 18: Microstructure of the degraded / non-printed sample after 56 days of exposure *Mix A*



505

506

*Figure 19: Closer view of the zone attained by the acid and the gypsum precipitation Mix A*

507  
508

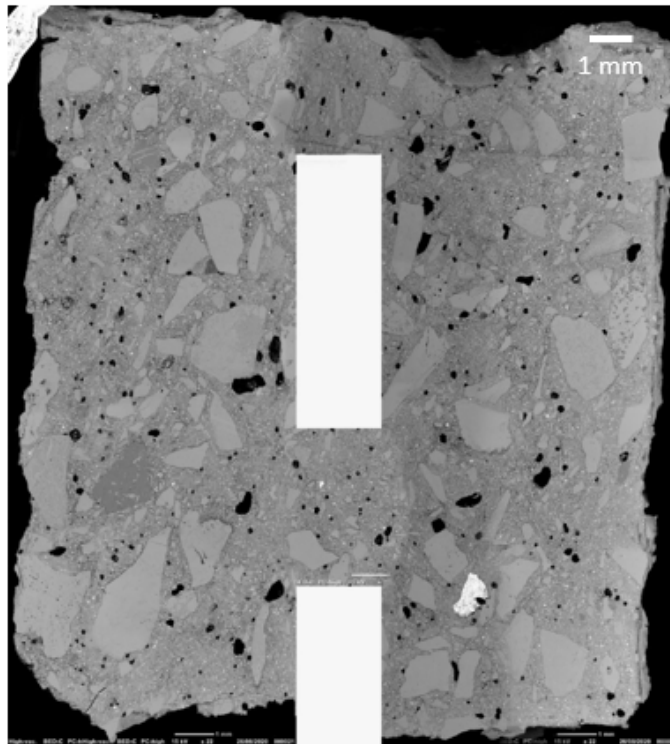


Figure 20: Microstructure of the degraded / printed sample Cut side 1 after 56 days of exposure **Mix A**

509  
510

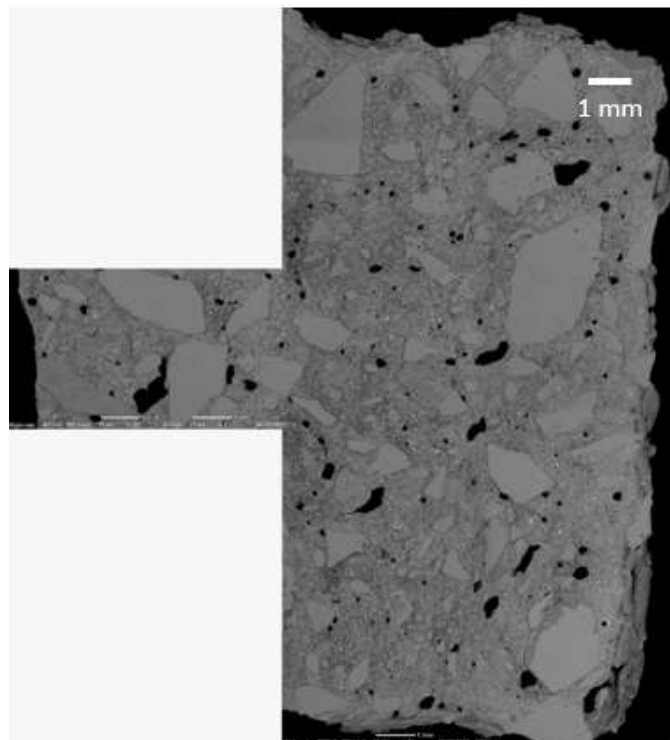


Figure 21: Microstructure of the degraded / printed sample Cut side 2 after 56 days of exposure **Mix A**

511 The findings of the SEM observations performed over all sample conditions (degraded / non-  
512 degraded, printed / non-printed) of Mix A were sufficient to figure out that no layers are going to  
513 appear in the rest mixes.

514 Moreover, as no inter-layers were perceived in the printed samples, it might be evident to say  
515 that the Mercury Intrusion Porosimetry performed over printed samples corresponds to that of  
516 the bulk material.

517 Overall, all these results including those of the MIP analysis confirmed the argument presented  
518 by De Koker [67] that in a printed concrete element, the concrete matrix could be denser than in  
519 a non-printed one, because of the external pressure exerted over the material when being  
520 extruded. Hence, this fact results in a stronger resistance against the degradation of the paste.

#### 521 4- Conclusion and perspectives

522 This article presents an experimental research aiming to characterize the microstructural  
523 properties of 3D printed concrete elements in regard to non-printed ones. In particular, a  
524 durability assessment has been carried out over three printable mortar mixes having different  
525 thixotropic properties. Herein, these samples were subjected to two sulfuric acid solutions of 1%  
526 and 3% concentrations for 56 days continuously.

527 First, a rheological characterization of the mortars used was carried out using the fall-cone  
528 penetrometer. The measurements revealed that the mixes under investigation covered a wide  
529 range of materials with different thixotropic properties.

530 Second on a macroscopic scale, a visual assessment was carried out for all samples of both  
531 exposures, and it was found the following:

- 532 • Printed and non-printed samples were equally deteriorated. However, those submerged in  
533 a 3% acid solution were much more degraded.
- 534 • The rate of mass loss between printed and non-printed samples of all mixes was almost  
535 the same, but still, the non-printed ones degrades slightly faster in most cases. This happened  
536 because of the presence of a larger number of accessible pores (for the same total volume of  
537 porosity) exposing a larger surface of paste. Nevertheless, printed samples did not fail at the inter-  
538 layer level or showed any cracks over that plane.

539 Third on a microscopic scale, only the samples of all mixes that were submerged in a solution of  
540 1% acid concentration were analyzed. This is done because the samples subject to 3% acid  
541 concentration were almost totally degraded. The porosity of all non-degraded samples, whether  
542 printed or not, were measured by the mercury intrusion porosimetry (MIP), and it was found the  
543 following:

- 544 • The total porosity of printed and non-printed samples of each mix separately was almost  
545 the same, however the pores size distribution varied a lot between printed and non-printed  
546 conditions. Generally, printed samples of all mixes presented a higher volume of pores having a  
547 diameter ranging between 1  $\mu\text{m}$  and 0.1  $\mu\text{m}$ . Despite that, non-printed samples showed the  
548 highest content of pores smaller than 0.1  $\mu\text{m}$ .

549 Besides, a scanning electron microscopy (SEM) visualization has been done over the degraded  
550 and non-degraded samples, in particular for Mix A that shows the highest level of surface  
551 roughness among all other mixes. Accordingly, the following conclusion was drawn:

552 • SEM clarified the pores size distribution triggered by the MIP, and confirmed the  
553 previous results.

554 • Despite of the material's thixotropic behavior, superposed layers are still able to merge  
555 together without showing any sign of layer stacking.

556 • Even when the printed samples were subjected to sulfuric acid attack, the inter-layers did  
557 not form weak planes for the solution ingress. Thus, the printed elements behaved as a  
558 monolithic body without showing any discontinuity in its internal structure that could threaten its  
559 durability.

560 Finally, it was perceived that the printing pressure applied over the material when being extruded  
561 has a fundamental effect of the material's internal structure. Hence it would be interesting to  
562 reconsider the same research context but by focusing on the effect of the printing parameters on  
563 the pore size distribution of a printed element, as well as their consequences on its durability  
564 against aggressive environments.

565

566

567

568 **Acknowledgment:**

569 The authors would like to acknowledge the financial support by Partenariats Hubert Curien  
570 (PHC) CEDRE program PROJET N° 42287YD, and the Supply of material from Carrières du  
571 Boulonnais, Eqiom, and Chryso.

- 572 [1] M. Stefanoni, U. Angst, and B. Elsener, “Corrosion challenges and opportunities in digital  
573 fabrication of reinforced concrete,” *1st RILEM Int. Conf. Concr. Digit. Fabr. Zurich,*  
574 *Switzerland.*, 2018.
- 575 [2] P. Wu, J. Wang, and X. Wang, “A critical review of the use of 3-D printing in the  
576 construction industry,” *Autom. Constr.*, vol. 68, pp. 21–31, 2016.  
577 DOI:10.1016/j.autcon.2016.04.005.
- 578 [3] G. De Schutter, K. Lesage, V. Mechtcherine, V. N. Nerella, G. Habert, and I. Agusti-Juan,  
579 “Vision of 3D printing with concrete — Technical, economic and environmental  
580 potentials,” *Cem. Concr. Res.*, vol. 112, pp. 25–36, 2018.  
581 DOI:10.1016/j.cemconres.2018.06.001.
- 582 [4] N. Labonnote, A. Rønquist, B. Manum, and P. Rüther, “Additive Construction: state of  
583 the art , challenges and opportunities,” *Autom. Constr.*, vol. 72, no. 3, pp. 347–366, 2016.  
584 DOI:10.1016/j.autcon.2016.08.026.
- 585 [5] J. Buchli, M. Gifftthaler, N. Kumar, M. Lussi, T. Sandy, K. Dör, and N. Hack, “Digital in  
586 situ fabrication - Challenges and opportunities for robotic in situ fabrication in  
587 architecture, construction, and beyond,” *Cem. Concr. Res.*, vol. 112, pp. 66–75, 2018.  
588 DOI:10.1016/j.cemconres.2018.05.013.
- 589 [6] B. Panda, C. Sonat, E.-H. Yang, M. J. Tan, and C. Unluer, “Use of magnesium-silicate-  
590 hydrate (M-S-H) cement mixes in 3D printing applications,” *Cem. Concr. Compos.*, vol.  
591 117, p. 103901, 2021. DOI:10.1016/j.cemconcomp.2020.103901.
- 592 [7] B. Panda, C. Sonat, E.-H. Yang, M. J. Tan, and C. Unluer, “Use of magnesium-silicate-  
593 hydrate (M-S-H) cement mixes in 3D printing applications,” *Cem. Concr. Compos.*, vol.  
594 117, p. 103901, 2021.
- 595 [8] J. J. Biernacki, J. W. Bullard, G. Sant, K. Brown, F. P. Glasser, S. Jones, T. Ley, R.  
596 Livingston, L. Nicoleau, J. Olek, F. Sanchez, R. Shahsavari, P. E. Stutzman, K. Sobolev,  
597 and T. Prater, “Cements in the 21<sup>st</sup> century: Challenges, perspectives, and opportunities,”  
598 *J. Am. Ceram. Soc.*, vol. 100, no. 7, pp. 2746–2773, 2017. DOI:10.1111/jace.14948.
- 599 [9] T. Wangler, E. Lloret, L. Reiter, N. Hack, F. Gramazio, M. Kohler, B. Mathias, D.  
600 Benjamin, J. Buchli, R. Nicolas, R. Flatt, and A. “Digital Concrete : Opportunities and  
601 Challenges,” *RILEM Tech. Lett.*, vol. 1, pp. 67–75, 2016.  
602 DOI:10.21809/rilemtechlett.2016.16.
- 603 [10] M. Sakin and Y. C. Kiroglu, “3D Printing of Buildings: Construction of the Sustainable  
604 Houses of the Future by BIM,” *Energy Procedia*, vol. 134, pp. 702–711, 2017.  
605 DOI:10.1016/j.egypro.2017.09.562.
- 606 [11] B. Nematollahi, M. Xia, and J. Sanjayan, “Current Progress of 3D Concrete Printing  
607 Technologies,” *Proc. 34th Int. Symp. Autom. Robot. Constr.*, pp. 260–267, 2017.  
608 DOI:10.22260/ISARC2017/0035.
- 609 [12] X. Zhang, I. Flood, Y. Zhang, H. I. Moud, and M. Hatami, “A Cost Model to Evaluate the  
610 Economic Performance of Contour Crafting,” *Comput. Civ. Eng. 2019 Vis. Inf. Model.*  
611 *Simul. - Sel. Pap. from ASCE Int. Conf. Comput. Civ. Eng. 2019*, no. June, pp. 618–625,

- 612 2019. DOI:10.1061/9780784482421.078.
- 613 [13] B. Panda and M. J. Tan, “Rheological behavior of high volume fly ash mixtures  
614 containing micro silica for digital construction application,” *Mater. Lett.*, vol. 237, pp.  
615 348–351, 2019. DOI:10.1016/j.matlet.2018.11.131.
- 616 [14] J. H. Lim, B. Panda, and Q. Pham, “Improving flexural characteristics of 3D printed  
617 geopolymer composite with in-process steel cable reinforcement reinforcement,” *Constr.*  
618 *Build. Mater.*, vol. 178, pp. 32–41, 2018. DOI:10.1016/j.conbuildmat.2018.05.010.
- 619 [15] F. Bos, R. Wolfs, Z. Ahmed, and T. Salet, “Additive manufacturing of concrete in  
620 construction: potentials and challenges of 3D concrete printing,” *Virtual Phys. Prototyp.*,  
621 vol. 11, no. 3, pp. 209–225, 2016. DOI:10.1080/17452759.2016.1209867.
- 622 [16] S. Z. Jones, J. Vickers, T. Wangler, and P. Zavattieri, “Additive Manufacturing Processes  
623 for Infrastructure Construction : A Review,” vol. 141, no. September, pp. 1–13, 2019.  
624 DOI:10.1115/1.4044106.
- 625 [17] S. Bukkapatnam, J. Mander, S. Paal, Z. Pei, and L. Zeng, “Workshop Report—NSF  
626 Workshop on Additive Manufacturing (3D Printing) for Civil Infrastructure Design and  
627 Construction,” *Natl. Sci. Found. (NSF)*, Alexandria, VA., 2017.
- 628 [18] “Winsun completes world’s first, 500 meters long, 3D printed river revetment wall.”  
629 [Online]. Available: [https://www.3dprintingmedia.network/winsun-completes-worlds-  
630 first-3d-printed-river-revetment-wall-in-largest-construction-3d-printing-project-yet/](https://www.3dprintingmedia.network/winsun-completes-worlds-first-3d-printed-river-revetment-wall-in-largest-construction-3d-printing-project-yet/).
- 631 [19] “In the Face of Climate Change: Saving Coral Reefs with 3D Printing.” [Online].  
632 Available:  
633 [https://www.engineering.com/3DPrinting/3DPrintingArticles/ArticleID/17809/In-the-  
634 Face-of-Climate-Change-Saving-Coral-Reefs-with-3D-Printing.aspx](https://www.engineering.com/3DPrinting/3DPrintingArticles/ArticleID/17809/In-the-Face-of-Climate-Change-Saving-Coral-Reefs-with-3D-Printing.aspx).
- 635 [20] D. Asprone, C. Menna, F. P. Bos, T. A. M. Salet, J. Mata-falcón, and W. Kaufmann,  
636 “Rethinking reinforcement for digital fabrication with concrete,” *Cem. Concr. Res.*, vol.  
637 112, pp. 111–121, 2018. DOI:10.1016/j.cemconres.2018.05.020.
- 638 [21] B. Baz, G. Aouad, N. Khalil, and S. Remond, “Inter - layer reinforcement of 3D printed  
639 concrete elements,” *Asian J. Civ. Eng.*, vol. 22, no. 2, pp. 341–439, 2020.  
640 DOI:10.1007/s42107-020-00317-0.
- 641 [22] B. BAZ, G. AOUAD, and S. REMOND, “Effect of the Printing Method and Mortar’s  
642 Workability on Pull-Out Strength of 3D Printed Elements,” *Constr. Build. Mater.*, vol.  
643 230, p. 117002, 2020. DOI:10.1016/j.conbuildmat.2019.117002.
- 644 [23] V. Mechtcherine, J. Grafe, V. N. Nerella, E. Spaniol, M. Hertel, and U. Füssel, “3D-  
645 Printed Steel Reinforcement for Digital Concrete Construction Manufacture, Mechanical  
646 Properties and Bond Behaviour,” *Constr. Build. Mater.*, vol. 179, pp. 125–137, 2018.  
647 DOI:10.13140/RG.2.2.33813.22248.
- 648 [24] R. N. P. Van Woensel, T. Van Oirschot, M. J. H. Burgmans, M. Mohammadi, Ph D, and  
649 K. Hermans, “Printing Architecture: An Overview of Existing and Promising Additive  
650 Manufacturing Methods and Their Application in the Building Industry,” *Int. J. Constr.*  
651 *Environ.*, vol. 9, no. 1, pp. 57–81, 2018. DOI:10.18848/2154-8587/cgp/v09i01/57-81.

- 652 [25] B. Baz, G. Aouad, P. Leblond, O. Al-mansouri, D. Melody, and S. REMOND,  
653 “Mechanical assessment of concrete – Steel bonding in 3D printed elements,” *Constr.*  
654 *Build. Mater.*, vol. 256, p. 119457, 2020. DOI:10.1016/j.conbuildmat.2020.119457.
- 655 [26] D. Lowke, E. Dini, A. Perrot, D. Weger, C. Gehlen, and B. Dillenburger, “Particle-bed 3D  
656 printing in concrete construction – Possibilities and challenges,” *Cem. Concr. Res.*, vol.  
657 112, pp. 50–65, 2018. DOI:10.1016/j.cemconres.2018.05.018.
- 658 [27] V. N. Nerella, H. Ogura, and V. Mechtcherine, “Incorporating reinforcement into digital  
659 concrete construction,” *Proc. IASS Symp. 2018, Creat. Struct. Des. July 16-20, 2018,*  
660 *MIN, Boston, USA*, pp. 1–8, 2018.
- 661 [28] R. A. Buswell and W. R. L. De Silva, “3D printing using concrete extrusion : a roadmap  
662 for research,” *Latex templates*, pp. 1–29, 2018.
- 663 [29] IMenaka G. Vitharana, S. C. Paul, S. Y. Kong, A. J. Babafemi, M. J. Miah, and B. Panda,  
664 “A study on strength and corrosion protection of cement mortar with the inclusion of  
665 nanomaterials,” *Sustain. Mater. Technol.*, vol. 25, p. e00192, 2020.  
666 DOI:10.1016/j.susmat.2020.e00192.
- 667 [30] W. Gao, Y. Zhang, D. Ramanujan, K. Ramani, Y. Chen, C. B. Williams, C. C. L. Wang,  
668 Y. C. Shin, S. Zhang, and P. D. Zavattieri, “The status , challenges , and future of additive  
669 manufacturing in engineering,” *Comput. Des.*, vol. 69, pp. 65–89, 2015.  
670 DOI:10.1016/j.cad.2015.04.001.
- 671 [31] I. Agustí-juan and G. Habert, “Environmental design guidelines for digital fabrication,” *J.*  
672 *Clean. Prod.*, vol. 142, pp. 2780–2782, 2017.
- 673 [32] Y. Tosun and R. Şahin, “DEVELOPMENTS OF 3D CONCRETE PRINTING  
674 PROCESS,” *Int. Civ. Eng. Archit. Conf. TRABZON / TURKEY*, 2019.
- 675 [33] B. Panda, S. Chandra Paul, and M. Jen Tan, “Anisotropic mechanical performance of 3D  
676 printed fiber reinforced sustainable construction material,” *Mater. Lett.*, vol. 209, pp. 146–  
677 149, 2017. DOI:10.1016/j.matlet.2017.07.123.
- 678 [34] G. Ma, J. Zhang, L. Wang, Z. Li, and J. Sun, “Mechanical characterization of 3D printed  
679 anisotropic cementitious material by the electromechanical transducer,” *Smart Mater.*  
680 *Struct.*, vol. 27, no. 7, 2018. DOI:10.1088/1361-665X/aac789.
- 681 [35] S. C. Paul, Y. W. D. Tay, B. Panda, and M. J. Tan, “Fresh and hardened properties of 3D  
682 printable cementitious materials for building and construction,” *Arch. Civ. Mech. Eng.*,  
683 vol. 18, no. 1, pp. 311–319, 2018. DOI:10.1016/j.acme.2017.02.008.
- 684 [36] E. Gallucci, K. Scrivener, A. Groso, M. Stampanoni, and G. Margaritondo, “3D  
685 experimental investigation of the microstructure of cement pastes using synchrotron X-ray  
686 microtomography ( $\mu$ CT),” *Cem. Concr. Res.*, vol. 37, no. 3, pp. 360–368, 2007.
- 687 [37] M. Moini, J. Olek, B. Magee, P. Zavattieri, and J. Youngblood, “Additive Manufacturing  
688 and Characterization of Architected Cement-based Materials via X-ray Micro-  
689 Computed Tomography,” *1st RILEM Int. Conf. Concr. Digit. Fabr. ETH, Zurich*, 2018.
- 690 [38] A. V Rahul, M. Santhanam, H. Meena, and Z. Ghani, “Mechanical characterization of 3D

- 691 printable concrete,” *Constr. Build. Mater.*, vol. 227, 2019.  
692 DOI:10.1016/j.conbuildmat.2019.116710.
- 693 [39] R. J. M. Wolfs, F. P. Bos, and T. A. M. Salet, “Hardened properties of 3D printed  
694 concrete: The influence of process parameters on interlayer adhesion,” *Cem. Concr. Res.*,  
695 vol. 119, pp. 132–140, 2019. DOI:10.1016/j.cemconres.2019.02.017.
- 696 [40] Y. Wei, D. Tay, Y. Wei, D. Tay, G. Heng, A. Ting, Y. Qian, B. Panda, and M. J. Tan,  
697 “Time gap effect on bond strength of 3D-printed concrete,” *Virtual Phys. Prototyp.*, pp. 1–  
698 10, 2018. DOI:10.1080/17452759.2018.1500420.
- 699 [41] B. Zareiyan and B. Khoshnevis, “Interlayer adhesion and strength of structures in Contour  
700 Crafting - Effects of aggregate size, extrusion rate, and layer thickness,” *Autom. Constr.*,  
701 vol. 81, pp. 112–121, 2017. DOI:10.1016/j.autcon.2017.06.013.
- 702 [42] B. Zareiyan and B. Khoshnevis, “Effects of interlocking on interlayer adhesion and  
703 strength of structures in 3D printing of concrete,” *Autom. Constr.*, vol. 83, pp. 212–221,  
704 2017. DOI:10.1016/j.autcon.2017.08.019.
- 705 [43] A. Akbar, S. Javid, P. Ghoddousi, G. G. Amiri, and K. Donyadideh, “A new  
706 photogrammetry method to study the relationship between thixotropy and bond strength of  
707 multi-layers casting of self- consolidating concrete,” *Constr. Build. Mater.*, vol. 204, pp.  
708 530–540, 2019. DOI:10.1016/j.conbuildmat.2019.01.204.
- 709 [44] J. G. Sanjayan, B. Nematollahi, M. Xia, and T. Marchment, “Effect of Surface Moisture  
710 on Inter-Layer Strength of 3D Printed Concrete,” *Constr. Build. Mater.*, vol. 172, pp. 468–  
711 475, 2018. DOI:10.1016/j.conbuildmat.2018.03.232.
- 712 [45] J. Van Der Putten, G. De Schutter, and K. Van Tittelboom, “The Effect of Print  
713 Parameters on the (Micro) structure of 3D Printed Cementitious Materials,” *RILEM*  
714 *Bookseries 19*, pp. 234–244, 2019.
- 715 [46] J. Van Der Putten, M. Deprez, V. Cnudde, and G. De Schutter, “Microstructural  
716 Characterization of 3D Printed Cementitious Materials,” *MDPI Mater.*, vol. 12, no. 18,  
717 2019.
- 718 [47] P. K. Mehta and P. J. M. Monteiro, “Concrete: Microstructure, Properties and Materials,”  
719 *3rd ed. McGraw-Hill, New York*, 2006.
- 720 [48] E. Hewayde, M. Nehdi, E. Allouche, and G. Nakhla, “Effect of Mixture Design  
721 Parameters and Wetting-Drying Cycles on Resistance of Concrete to Sulfuric Acid  
722 Attack,” *J. Mater. Civ. Eng.*, vol. 19, no. 2, pp. 155–163, 2007.
- 723 [49] “BS EN 206:2013 Concrete — Specification , performance , production and conformity,”  
724 2014.
- 725 [50] L. Gu, T. Bennett, and P. Visintin, “Sulphuric acid exposure of conventional concrete and  
726 alkali-activated concrete : Assessment of test methodologies,” *Constr. Build. Mater.*, vol.  
727 197, pp. 681–692, 2019. DOI:10.1016/j.conbuildmat.2018.11.166.
- 728 [51] S. Barbhuiya and D. Kumala, “Behaviour of a Sustainable Concrete in Acidic  
729 Environment,” *MDPI Sustain.*, vol. 9, no. 1556, 2017. DOI:10.3390/su9091556.

- 730 [52] E. Mene´ndez, T. Matschei, and F. P. Glasser, “Sulfate Attack of Concrete,” *Perform.*  
731 *Cem. Mater. Aggress. Aqueous Environ. RILEM State-of-the-Art Reports 10*, 2013.  
732 DOI:10.1007/978-94-007-5413-3.
- 733 [53] K. Kawai, S. Yamaji, and T. Shinmi, “Concrete Deterioration Caused by Sulfuric Acid  
734 Attack,” *10DBMC Int. Conférence Durab. Build. Mater. Components LYON [France]*,  
735 2005.
- 736 [54] P. Tinghong, Y. Jiang, H. He, Y. Wang, and K. Yin, “Effect of Structural Build-Up on  
737 Interlayer Bond Strength of 3D,” *Materials (Basel)*, vol. 14, no. 2, p. 263, 2021.  
738 DOI:10.3390/ma14020236.
- 739 [55] Y. Wei, D. Tay, M. Y. Li, and M. J. Tan, “Effect of printing parameters in 3D concrete  
740 printing : Printing region and support structures,” vol. 271, pp. 261–270, 2019.  
741 DOI:10.1016/j.jmatprotec.2019.04.007.
- 742 [56] B. Panda, N. Ahamed, N. Mohamed, S. C. Paul, G. V. P. B. Singh, M. J. Tan, and B.  
743 Šavija, “The Effect of Material Fresh Properties and Process Parameters on Buildability  
744 and Interlayer Adhesion of 3D Printed Concrete,” *Mater.*, vol. 12, no. 13, p. 2149, 2019.  
745 DOI:10.3390/ma12132149.
- 746 [57] B. A. Baz, S. Remond, and G. Aouad, “Influence of the mix composition on the  
747 thixotropy of 3D printable mortars,” *Mag. Concr. Res.*, 2020.  
748 DOI:10.1680/jmacr.20.00193.
- 749 [58] K. El Cheikh, S. Rémond, N. Khalil, and G. Aouad, “Numerical and experimental studies  
750 of aggregate blocking in mortar extrusion,” *Constr. Build. Mater.*, vol. 145, pp. 452–463,  
751 2017. DOI:10.1016/j.conbuildmat.2017.04.032.
- 752 [59] “AFNOR NF EN 196-1, Methods of testing cement - Part 1 : determination of strength,”  
753 2006.
- 754 [60] CEN (European Committee for Standardization), “EN ISO 17892-6: Geotechnical  
755 investigation and testing - laboratory testing of soil - part 6: Fall cone test,” 2017.
- 756 [61] P. Estellé, C. Michon, C. Lanos, and J. L. Grossiord, “De l ’ intérêt d ’ une caractérisation  
757 rhéologique empirique et relative,” *Rhéologie*, vol. 21, pp. 10–35, 2012.
- 758 [62] N. Roussel, “A thixotropy model for fresh fluid concretes : Theory , validation and  
759 applications,” *Cem. Concr. Res.*, vol. 36, pp. 1797–1806, 2006.  
760 DOI:10.1016/j.cemconres.2006.05.025.
- 761 [63] A. Luisa, T. Torres, and M. Isabel, “Concrete degradation mechanisms by sulfuric acid  
762 attack,” *Mag. Concr. Res.*, vol. 71, no. 7, pp. 1–13, 2018. DOI:10.1680/jmacr.18.00194.
- 763 [64] “ASTM C1012/C1012M – 18b Standard Test Method for Length Change of Hydraulic-  
764 Cement Mortars Exposed to a Sulfate Solution,” pp. 1–9, 2018. DOI:10.1520/C1012.
- 765 [65] F. Gong, D. Zhang, E. Sicat, and T. Ueda, “Empirical Estimation of Pore Size Distribution  
766 in Cement , Mortar , and Concrete,” *Mater. Civ. engoneering*, vol. 26, no. 7, 2014.  
767 DOI:10.1061/(ASCE)MT.1943-5533.0000945.

- 768 [66] A. Perrot, D. Rangeard, and A. Pierre, "Structural built-up of cement-based materials used  
769 for 3D- printing extrusion techniques," *Mater. Struct.*, vol. 49, pp. 1213–1220, 2016.  
770 DOI:10.1617/s11527-015-0571-0.
- 771 [67] D. De Koker, "Manufacturing processes for engineered cement-based composite material  
772 products," *M.Sc. thesis, Stellenbosch Univ. South Africa*, 2004.
- 773 [68] C. Schr and V. N. Nerella, "Capillary Water Intake by 3D-Printed Concrete Visualised  
774 and Quantified by Neutron Radiography," *First RILEM Int. Conf. Concr. Digit. Fabr. –*  
775 *Digit. Concr. 2018*, pp. 217–224, 2018. DOI:10.1007/978-3-319-99519-9.
- 776 [69] J. Van Der Putten, G. De Schutter, and K. Van Tittelboom, "The Effect of Print  
777 Parameters on the (Micro)structure of 3D Printed Cementitious Materials," *First RILEM*  
778 *Int. Conf. Concr. Digit. Fabr. – Digit. Concr. 2018*, pp. 234–244, 2018.
- 779 [70] P. C. Bran Anleu, T. Wangler, and R. J. Flatt, "Chloride Ingress Through Cold Joints in  
780 Digitally Fabricated Concrete by micro-XRF Mapping," *First RILEM Int. Conf. Concr.*  
781 *Digit. Fabr. – Digit. Concr. 2018*, 2018.
- 782